

# Computational Role of Collective Tunneling in a Quantum Annealer

Sergio Boixo<sup>1</sup>, Vadim N. Smelyanskiy<sup>2</sup>, Alireza Shabani<sup>1</sup>, Sergei V. Isakov<sup>1</sup>, Mark Dykman<sup>3</sup>, Vasil S. Denchev<sup>1</sup>, Mohammad Amin<sup>4</sup>, Anatoly Smirnov<sup>4</sup>, Masoud Mohseni<sup>1</sup>, Hartmut Neven<sup>1</sup>

<sup>1</sup>*Google, Venice, CA 90291, USA*

<sup>2</sup>*NASA Ames Research Center, Moffett Field, CA 94035, USA*

<sup>3</sup>*Department of Physics and Astronomy, Michigan State University, East Lansing, MI 48824, USA*

<sup>4</sup>*D-Wave Systems Inc., Burnaby, BC V5C 6G9, Canada*

Quantum tunneling is a phenomenon in which a quantum state traverses energy barriers above the energy of the state itself [1, 2]. Tunneling has been hypothesized as an advantageous physical resource for optimization [3–7]. Here we present the first experimental evidence of a computational role of multiqubit quantum tunneling in the evolution of a programmable quantum annealer. We develop a theoretical model based on a NIBA Quantum Master Equation to describe the multiqubit dissipative tunneling effects under the complex noise characteristics of such quantum devices. We start by considering a computational primitive, an optimization problem consisting of just one global and one false minimum. The quantum evolutions enable tunneling to the global minimum while the corresponding classical paths are trapped in a false minimum. In our study the non-convex potentials are realized by frustrated networks of qubit clusters with strong intra-cluster coupling. We show that the collective effect of the quantum environment is suppressed in the “critical” phase during the evolution where quantum tunneling “decides” the right path to solution. In a later stage dissipation facilitates the multiqubit tunneling leading to the solution state. The predictions of the model accurately describe the experimental data from the D-Wave Two quantum annealer at NASA Ames. In our computational primitive the temperature dependence of the probability of success in the quantum model is opposite to that of the classical paths with thermal hopping. Specifically, we provide an analysis of an optimization problem with sixteen qubits, demonstrating eight qubit tunneling that increases success probabilities. Furthermore, we report results for larger problems with up to 200 qubits that contain the primitive as subproblems.

## I. INTRODUCTION

Quantum tunneling was discovered in the late 1920s to explain radioactive decay [1] and field electron emission in vacuum tubes [2]. Today this phenomenon is at the core of many essential technological innovations such as the tunnel field-effect transistor [8], field emission displays and the scanning tunneling microscope [9]. Tunneling also plays a key role in energy and charge transport in biological and chemical processes [10]. Recently, tunneling effects involving multiple quantum mechanical particles have been used to develop single electron transistors [11] and hypersensitive measurement instruments.

Collective tunneling phenomenon plays a central role in switching between stable states of molecular nanomagnets [12–15]. These bistable units locally connected to each other are studied as building blocks for magnetic cellular automata [16] and digital integrated circuits [17]. The tunneling behavior there is displayed by ferromagnetic clusters with large spins (of size ten [18] and more [19]) formed by individual ion spins moving as a whole under the collective energy barrier due to a strong exchange forces between them.

Quantum tunneling, in particular for thin but high energy barriers, has been hypothesized as an advantageous mechanism for quantum optimization [3–7, 20]. In classical simulated annealing or cooling optimization algorithms, the corresponding temperature parameter must be raised to overcome energy barriers. But if there are many potential local minima with smaller energy differences than the height of the barrier, the temperature must also be lowered to distinguish between them so the algorithm can converge to

the global minimum. Quantum tunneling is present even at zero-temperature. Therefore, for some energy landscapes, one might expect that quantum dynamical evolutions can converge to the global minimum faster than classical optimization algorithms. Quantum annealing [3, 4] is a technique inspired by classical annealing but designed to take advantage of quantum tunneling. Single qubit quantum tunneling for a programmable annealer has been demonstrated experimentally in Ref. [21], and two qubit tunneling has been detected indirectly using microscopic resonant tunneling in Ref. [22].

In the idealized limit of quantum annealing the dynamics of the system is unitary and evolves adiabatically under a slowly varying time-dependent Hamiltonian. The system will arrive at the final ground state of the problem Hamiltonian if the total evolution time is large compared to the inverse minimum energy gap along the Hamiltonian path [23]. In this paper, we shall analyze the performance of a quantum annealing device with superconducting flux qubits [21, 24, 25]. The qubits are coupled inductively in a connectivity graph that is formed by a grid of cells with high internal connectivity. The qubits are subject to interaction with the environment with the dominant noise source being spin diffusion at the superconductor insulator interface [26–28]. This is known to produce control errors, energy level broadening as well as thermal excitation and relaxation [29, 30]. The noise characteristics of individual qubits have been studied in macroscopic resonant tunneling experiments [31]. We show nevertheless that even under such conditions the device performance can benefit from multiqubit tunneling of strongly interacting qubit clusters. This is of relevance for current programmable quantum annealers, such as

the D-Wave Two chip at NASA Ames.

The performance of D-Wave’s quantum annealers has been studied in a number of recent works [21, 25, 32–46]. Results from a D-Wave quantum annealer chip are very different from models that do not quantize the superconducting flux qubits [21, 32, 36]. It has also been shown that under current noise parameters it is possible to prepare entangled states of eight qubits, using static Hamiltonians with a gap much bigger than the temperature [37]. A good correlation with a classical-path model [47] (see Sec. III D) has been observed for a benchmark of random Ising instances [41], as well as differences in distributions of excited states or degenerate ground states [42, 45].

Reference [33] makes the interesting observation that for a problem instance with energy gap much smaller than the temperature (and without false minima) the probability of success increases with temperature. In these conditions, noise effects are very strong and they destroy coherent quantum superpositions. The system actually resides in (classical) product states making random hoppings between them. In contrast, we will introduce instances where fast collective tunneling processes of many qubits give rise to correlated quantum superposition states [37]. Multiple qubit tunneling will play a significant role both in the formation of the dynamical states themselves and in giving rise to a large transition rate between these states. For these instances we obtain an opposite temperature dependence behavior: decreasing probability of success with increasing temperature. This is in contrast with the limit of incoherent tunneling or to the classical-path model.

In this work we design an Ising model implementation with 16 qubits of a computational primitive, the simplest non-convex optimization problem consisting of just one global and one local minimum. The final global minimum can only be reached by traversing an energy barrier. We develop a NIBA Quantum Master Equation which takes high and low frequency noise into account. Our comprehensive open quantum system modeling shows close agreement with experiments conducted using the D-Wave device and demonstrates how collective tunneling can exist and play a computational role in the presence of both Ohmic and strong  $1/f$  noise affecting flux qubit coherence. Quite generally, our model predicts that the probability to find the system in the lowest energy state should decrease with temperature for a quantum system and increase with temperature for a classical system. Consistent with the quantum model, we show that temperature and success probability are inversely related in a series of 16 qubit D-Wave experiments. We compare with alternative physically plausible models of the hardware that only employ product states and do not allow for multiqubit tunneling transitions. Experimentally, we show that the D-Wave Two processor has a higher success probability than any of these models for a series of problems. We also explore larger problems embedded on 200 qubits that contain multiple weak-strong cluster pairs. We observe that the success probabilities of quantum annealing outperform the models that, for physically motivated parameter regimes, rely on clas-

sical paths to the solution.

## II. A PRIMITIVE “PROBE” PROBLEM

### A. The quantum Hamiltonian

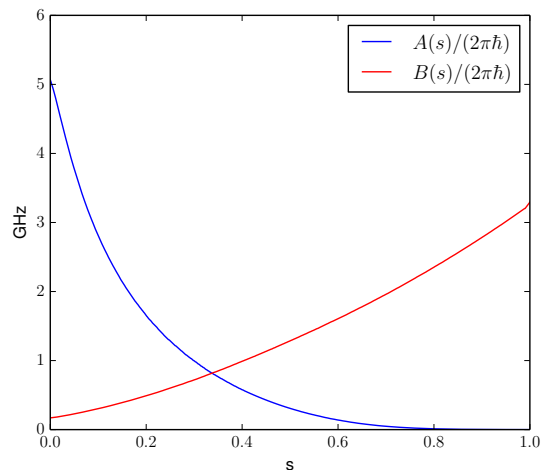


FIG. 1. Quantum annealing functions  $A(s)$  and  $B(s)$ . The function  $A(t)$  is defined as half the median energy difference between the two lowest eigenstates of the experimentally superconducting flux qubit with zero bias. The function  $B(s)$  is defined as 1.41 pico henries times the square of the persistent current  $I_p^2(s)$ , as explained in App. II C Eq. (A14).

The state evolution in transverse field quantum annealing is governed by a time dependent Hamiltonian of the form [23]

$$H_0(s) = A(s)H^D + B(s)H^P \quad (1)$$

$$H^D = - \sum_{\mu} \sigma_{\mu}^x \quad (2)$$

$$H^P = - \sum_{\mu} h_{\mu} \sigma_{\mu}^z - \sum_{\mu\nu} J_{\mu\nu} \sigma_{\mu}^z \sigma_{\nu}^z. \quad (3)$$

Here  $H^D$  is the driver Hamiltonian,  $H^P$  is the problem Hamiltonian whose ground state is the solution of an optimization problem of interest,  $\{\sigma_{\mu}^x, \sigma_{\mu}^z\}$  are Pauli matrices acting on spin  $\mu$ ,  $s = t/t_{qa}$  is the annealing parameter, and  $t_{qa}$  is the duration of the quantum annealing process. The functions  $A(s)$  and  $B(s)$  used in the rest of the paper are shown in Fig. 1. The Hamiltonian path  $H_0(s)$  describes an evolution of effective 2-level spin systems (qubits) from an initial phase with a unique ground state to a final Hamiltonian with eigenstates aligned with the  $z$  quantization axis. In the initial unique ground state all the qubits are aligned with the effective transverse magnetic field in the  $x$  direction. See Appendix A for a more complete derivation of the single qubit Hamiltonian and the parameters of the experimental system considered in this paper.

## B. The weak-strong cluster “probe” Hamiltonian

The canonical primitive to study quantum tunneling is a double-well potential: two local minima separated by an energy barrier. Our aim is to distinguish quantum tunneling from thermal activation in a model using classical paths. Classical paths are limited to local spin vector dynamics over product states to traverse the barrier. In contrast, the signature of a quantum system is that entangled states are available as well. We utilize qubit networks of the D-Wave Two quantum annealer at NASA Ames to design time-dependent asymmetric double-well potentials where a classical path continuously connects the initial global minimum to the final false minimum. In this way, one can study how the system escapes the local minimum and traverses the energy barrier to reach the global optimum. We will see that quantum tunneling results in a different final probability of success than the corresponding dynamics over classical paths. We compare the experimental data from the device with numerical simulations of these classical paths and with the predictions of a comprehensive analytical model for dissipative multiqubit tunneling. Based on the results of this comparison, we establish a functional role of tunneling in the evolution of a programmable quantum annealer.

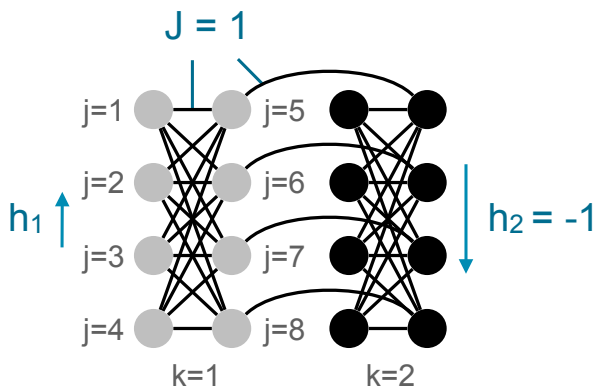


FIG. 2. The probe problem under study, consisting of 16 qubits in two unit cells of the so-called Chimera graph. All qubits are ferromagnetically coupled and evolve as two distinct qubit clusters. At the end of the annealing evolution the right cluster is strongly pinned downward due to strong local fields acting on all qubits in that cell. However, the local magnetic field  $h_1$  in the left cluster is weaker and serves as a bifurcation parameter. For  $h_1 < J/2$  the left cluster will reverse its orientation during the annealing sweep and eventually align itself with the right cluster. Note the permutation symmetry in each column which allows us to adopt the large spin description.

We now detail how the double-well potential and time evolution can be constructed in the case of network graphs with finite connectivity. We will focus on the particular case of the so-called Chimera graph that connects the qubits in the current D-Wave Two architecture, although similar constructions can be applied to more general network architectures. We choose our double-well primitive probe problem to be the one de-

picted in Fig. 2. We use two Chimera cells, each with  $n = 8$  qubits. We find it useful during our analysis to keep  $n$  explicit. We will choose equal local fields for the spins within each cell. We also choose all the couplings to be equal and ferromagnetic. The problem Hamiltonian is of Ising form

$$H^P = H_1^P + H_2^P + H_{1,2}^P \quad (4)$$

$$H_k^P = -J \sum_{\langle j,j' \rangle \in \text{intra}} \sigma_{k,j}^z \sigma_{k,j'}^z - \sum_{j=1}^n h_k \sigma_{k,j}^z \quad (5)$$

$$H_{1,2}^P = -J \sum_{j \in \text{inter}} \sigma_{1,j}^z \sigma_{2,j}^z. \quad (6)$$

The index  $k \in \{1, 2\}$  denotes the Chimera cell, the first sum in (5) goes over the *intra*-cell couplings depicted in Fig. 2, and the second sum goes over the *inter*-cell couplings corresponding to  $j \in (n/2 + 1, n)$  in Fig. 2;  $h_k$  denotes the local fields within each cell.

Toward the end of quantum annealing the problem Hamiltonian  $H^P$  is dominating the evolution and  $\langle \sigma_{k,j}^z \rangle \simeq \pm 1$  where here  $\langle \dots \rangle$  denotes a quantum mechanical average. There are  $n^2/4$  *intra*-cell couplings and  $n/2$  *inter*-cell couplings. The spins within each cell tend to move together as an homogenous cluster because flipping only one spin rises the energy by an amount  $\propto nJ$  which is much greater than the energy of the inter-cell bond  $\propto 2J$ . Therefore the low lying states of  $H_P$  correspond to the spins in each cluster pointing in the same direction (see Fig. 3). In the first two states the second cluster is pointing along its own local field  $h_2 < 0$  (largest in magnitude field). The difference in energy of the states with both clusters pointing in the opposite and the same directions equals

$$E_{\uparrow\downarrow} - E_{\downarrow\downarrow} = 2n(J/2 - h_1) \quad (7)$$

If  $h_1 < J/2$  then the global minimum corresponds to both clusters having the same orientation as the largest magnitude field,  $h_2$ . The next energy level (a “false” minimum) corresponds to the clusters oriented in the opposite directions (each along its own local field).

We now explain the onset of frustration in this system. We observe that at the beginning of quantum annealing

$$\langle \sigma_{k,j}^z \rangle \simeq h_k B(s)/A(s), \quad B(s)/A(s) \ll 1. \quad (8)$$

The Ising coupling terms in the problem Hamiltonian (5) are quadratic while the local field terms are linear in  $z$ -polarizations. Therefore at the beginning of quantum annealing the effect of the local  $z$ -fields dominates that of the *inter*-cell Ising couplings. According to (8), because  $h_1$  and  $h_2$  have the opposite signs so will the  $z$ -projections of the spins  $\langle \sigma_{k,j}^z \rangle$  in the two clusters early in the evolution.

A key observation is that in the absence of quantum tunneling and thermal hopping, the spin projection of the two clusters stay opposite during the evolution. The system would arrive to the false minimum with residual energy relative to the global minimum equal to  $n(J - 2h_1)$ ; i.e. it will get trapped in the false

minimum. To escape the false trap, all spins in the left cluster must flip sign, which requires traversing the barrier. At its peak, the barrier trapping the left cluster has zero total z-polarization and therefore the barrier grows with the ferromagnetic energy of the cluster  $(n/2)^2 J$ . For sufficiently large  $n$ , the barrier height  $\mathcal{O}(n^2)$  is much greater than the residual energy  $\mathcal{O}(n)$ . It will be shown below that (for certain values of the annealing parameter  $s$ ), all qubits in the left cluster will tunnel in a concerted motion under the energy barrier separating the two potential wells that correspond to the opposite z-polarizations of the cluster.

Next, we discuss an approximation which reduces the size of the Hamiltonian matrix for the 2 unit cell problem from  $2^{2n}$  to  $(n/4 + 1)^4$ . We introduce total spin operators for each column of a unit cell (cf. Fig. 2)

$$S_{k,1}^\alpha = \frac{1}{2} \sum_{j=1}^{n/2} \sigma_{k,j}^\alpha, \quad S_{k,2}^\alpha = \frac{1}{2} \sum_{j=n/2+1}^n \sigma_{k,j}^\alpha, \quad (9)$$

where  $\alpha \in \{x, y, z\}$ , and  $k \in \{1, 2\}$  denotes the left and right Chimera cells. Because the intra-cell Hamiltonians (5) and the driver Hamiltonian are symmetric with respect to qubit permutations they can be written in terms of the total spin operators

$$\begin{aligned} H_k^P &= -4JS_{k,1}^z S_{k,2}^z - 2h_k S_k^z & (10) \\ H^D &= -2 \sum_{k,m=1,2} S_{k,m}^x. \end{aligned}$$

We note that the inter-cell Hamiltonian  $H_{1,2}^P$  in Eq. (6) does not possess the qubit permutation symmetry. However, as explained above, the qubits in each cell tend to evolve as homogenous clusters. Therefore one can approximate the inter-cell Hamiltonian in terms of the total spin operators for the columns

$$H_{1,2}^P \simeq -\frac{8}{n} JS_{1,2}^z S_{2,2}^z. \quad (11)$$

We observe that the system Hamiltonian commutes with the total spin operators  $S_{k,m}^2 = \sum_{\alpha \in \{x,y,z\}} (S_{k,m}^\alpha)^2$ . Given that all qubits in the initial state are polarized along the x-axis, this restricts the evolution to the subspace of maximum total spin values  $n/4$  for each column. This subspace is spanned by the basis vectors  $|n/4, m_{k,m}\rangle$  corresponding to the definite projections of column spins on the z axis  $m_{k,m} = -n/4, \dots, n/4$ . As a measure of the error incurred by this approximation, it can be seen that the two lowest energy levels are within 0.1% of the exact values for the case of interest,  $n = 8$ .

### C. Effective energy potential for the classical paths of product states

We now derive the effective potential over product states used to study the difference between thermal hopping among classical paths, and quantum tunneling in the quantum models. This will also serve to

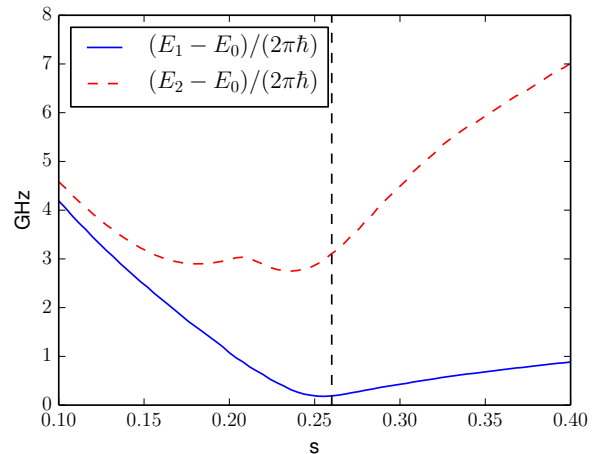


FIG. 3. Gap of the quantum Hamiltonian for  $h_1 = 0.44$  as a function of the annealing parameter. The continuous line is the energy difference between the ground state and the first excited state. The avoided crossing at  $s = 0.26$  (dashed vertical line) corresponds to a minimum gap of 180 MHz. The dashed line is the energy difference between the ground state and the second excited state.

clarify the tunneling picture described above. We first transform to a representation that contains an explicit momentum operator. We think of each cluster  $k$  as a spin- $n/2$  ferromagnetic “particle” with the coordinate proportional to its total spin z projection  $\sum_{j=1,2} S_{k,j}^z$ . Because the x-component of the total spin of the cluster does not commute with the z-component it is naturally associated with the momentum that causes the particle to move. This allows us to think of the z-component of a large spin as a particle moving in a slowly time-varying potential, formalizing the cartoon pictures sometimes drawn to illustrate quantum annealing that show a particle escaping a local minimum in a continuous potential via tunneling. This picture is also very similar to that of the dynamics of large spin magnetic moment molecular materials [14].

The canonically conjugate coordinate and momenta operators can be naturally introduced within the WKB framework (see App. B)

$$S_{k,1}^z + S_{k,2}^z = \frac{n}{2} q_k \quad (12)$$

$$S_{k,1}^x + S_{k,2}^x \approx \frac{n}{2} \sqrt{1 - q_k^2} \cos p_k \quad (13)$$

where  $[q, p] = i(2/n)$  and  $2/n \ll 1$  plays the role of Planck’s constant in traditional WKB. To the leading order in  $1/n$  the Hamiltonian becomes

$$\begin{aligned} H^{\text{WKB}}(q_1, q_2, p_1, p_2, s) &= -nA(s) \sum_{k=1,2} \sqrt{1 - q_k^2} \cos p_k \\ &- nB(s)J \sum_{k=1,2} \left( h_k q_k + nq_k^2/4 \right) - \frac{n}{2} B(s)J q_1 q_2. \end{aligned} \quad (14)$$

The above Hamiltonian describes a pair of coupled ferromagnetic particles each with spin  $n/2$ . WKB theory based on this Hamiltonian describes eigenstates and

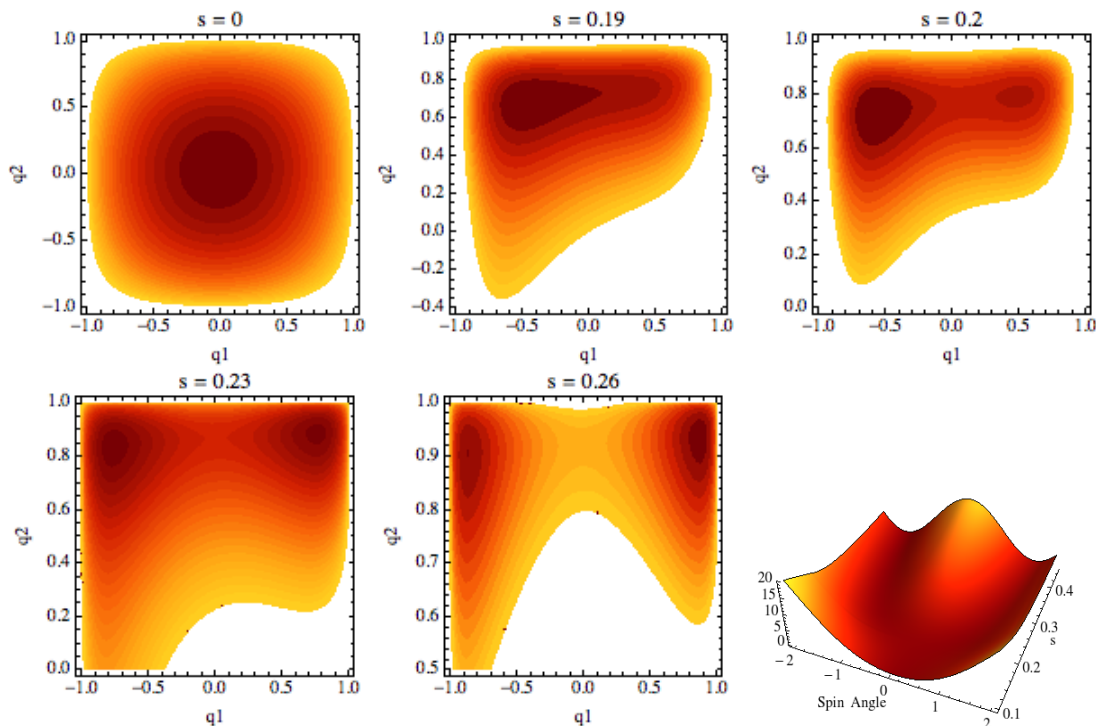


FIG. 4. The five snapshots in this figure show how the energy landscape  $U(q_1, q_2)$  evolves and a double-well potential is formed during the annealing schedule. The 3D plot also depicts such evolution as a function of an effective orientation angle for the large spins. The minimum that forms first would trap a classical particle moving in this potential. Later in the annealing evolution a second minimum forms and eventually becomes the global minimum. To reach this global minimum the system state has to traverse the energy barrier between them. The origin of this bifurcation is explained in the text.

eigenvalues with logarithmic accuracy in the asymptotic limit  $n \gg 1$ . It also gives a reasonable estimates already for  $n = 8$  (see App. B).

We will now consider the potential corresponding to a low energy description with very low momenta

$$U(q_1, q_2, s) = H^{\text{WKB}}(q_1, q_2, 0, 0, s) \quad (15)$$

The same potential is obtained in Ref. [6] projecting the Hamiltonian of large spin operators Eqs. (10), (11) over spin coherent states, which are product states. The different panels in Figure 4 depict the potential  $U(q_1, q_2)$  for different values of the annealing parameter  $s$  with local field  $h_1 = 0.44$ . Initially ( $s = 0$ ) there is only a global minimum at  $q_1 = q_2 = 0$  corresponding to all spins aligned with the x-direction. As  $s$  grows the minima begins to move to the left corner  $(-1, 1)$  corresponding to the opposite orientations of the clusters. This effect was previously mentioned in the general context. The terms in the effective potential corresponding to the local fields  $h_k$  are linear in  $q_k$ , and dominate the Ising coupling energy (quadratic in  $q_k$ ) between the large spins for  $|q_k| \ll 1$ . For larger values of  $s$  the Ising terms begin to compete with the local fields and a plateau is formed in the vicinity of  $q_1 = 0$  following the local bifurcation of  $U$  and giving rise to a new minimum corresponding to the ferromagnetic alignment of the two clusters. At some value  $s_c$  the two minima coexist with equal energy. For  $s > s_c$  the minimum corresponding to the ferromagnetic cluster alignment has a lower energy, smoothly connecting to the solution state at the end of quantum annealing,

corresponding to the global minimum of the potential  $U(q_1, q_2, s = 1)$  at  $q_1 = q_2 = 1$ .

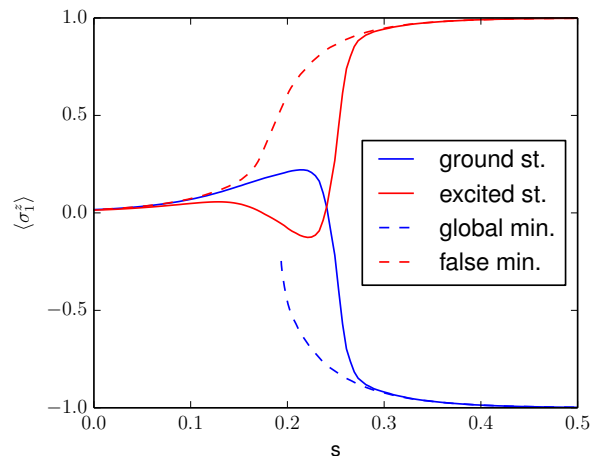


FIG. 5. Solid lines show the  $z$ -magnetization  $\langle \sigma_1^z \rangle$  for the quantum ground state and first excited state as a function of the annealing parameter  $s$  for  $h_1 = 0.44$ . Dashed lines show the value of  $q_1$  along the paths corresponding to the false and global minima for the effective energy potential over product states. The correspondence is good, except at the avoided crossing where the quantum states are entangled.

In a closed system, the quantum adiabatic evolution algorithm allows the system to tunnel from the old global minimum to the new one in the vicinity of  $s_c$  [6].



It tunnels under a barrier whose maximum approximately corresponds to zero z-magnetization  $q_1 = 0$ . The tunneling corresponds to an avoided crossing between the two lowest energy levels of the Hamiltonian  $H_0(s)$  of Eq. (1) shown in Fig. 3. During tunneling, the total spin of the left cluster switches its direction. The switching manifests itself in Fig. 5 as a steep change in  $s$ -dependence of the quantum mechanical average of the left cluster polarization  $\langle q_1 \rangle$  in the instantaneous ground state. In contrast, the right cluster, which does not tunnel, displays a smooth change in its average polarization  $\langle q_2 \rangle$ .

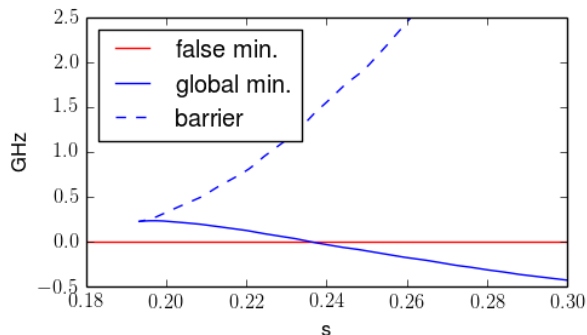


FIG. 6. Bifurcation for  $h_1 = 0.44$ . The energies of the paths of the double-well minima and the height of the effective energy barrier are plotted in GHz and we have subtracted off the instantaneous energy of the final false minimum. The path corresponding to the global minimum appears as a bifurcation with higher energy. When this path crosses the path of the final false minimum, the height of the energy barrier is substantial.

In classical dynamical evolutions, when tunneling is not possible, the system will continue to reside in the initial global minimum emanating from the point  $(0, 0)$ . Fig. 6 shows the energies of the two classical paths corresponding to the two minima of the energy potential  $U(q_1, q_2, s)$  for  $h_1 = 0.44$ . Classical dynamical evolutions will get trapped in the false minimum path due to the bifurcation seen in this figure. Classical trajectories can only reach the global minimum through thermal excitations. In Figure 5 we also show the value of the parameter  $q_1$  corresponding to the local minima of  $U(q_1, q_2, s)$  as a function of the annealing parameter  $s$ . The parameter  $q_1$  for the classical path connecting to the final false minimum first aligns with the quantum ground state and later aligns with the quantum first-excited state. This path starts at the point  $(q_1, q_2) = (0, 0)$ . The bifurcation path corresponding to the global minimum first appears with a definite but small  $q_1$ , and later aligns with the quantum ground state after the avoided crossing.

### III. MODELING THE ANNEALING DYNAMICS

#### A. Characterization of noise and dissipation

Under realistic conditions, the performance of a quantum annealer as an optimizer can be strongly in-

fluenced by the coupling to the environment. In order to capture this effect we present a *phenomenological* open quantum system model by incorporating the experimental characterization of the noise that was performed to date on D-Wave devices (the experimental platform for the present investigation).

We shall assume that each flux qubit is coupled to its own environment with an independent noise source; this assumption is consistent with experimental data [22]. We separate the bath excitations into two parts. Excitations with frequencies lower than the annealing rate in our experiments (5 KHz) will be treated as a “static noise” whose effect can be included by an appropriate averaging of the success rate over the local field errors ( $\sim 5\%$  for the D-Wave Two chip). The excitations with higher frequencies will be modeled as a bath of harmonic oscillators. This approach is quite general and independent of the true physical source of the noise. Its validity rests on the assumptions that the free bath (decoupled from the qubits), is in thermal equilibrium, that it can be treated within the conditions of linear response theory, and that it has Gaussian fluctuations [48]. The corresponding system-bath Hamiltonian is

$$H(s) = H_0(s) + \frac{1}{2} \sum_{\mu=1}^{2n} \sigma_{\mu}^z Q_{\mu}(s) + H_B, \quad s = t/t_{qa}. \quad (16)$$

Hereafter we will use for brevity a single index  $\mu$  for single-qubit Pauli matrices instead of the double indexation employed in Sec. II. In the equation above,  $t_{qa}$  is the duration of the quantum annealing process,  $H_0(t)$  is the Hamiltonian for the  $2n$ -qubit system (as in Eq. (1)),  $H_B$  is the standard Hamiltonian of the bosonic bath, and  $Q_{\mu}(s)$  is a bosonic noise operator that couples the  $\mu^{\text{th}}$  qubit to its environment. The coupling parameters of bosonic bath operator  $Q_{\mu}(s)$  depend on the annealing parameter  $s$  through the persistent current (see App. A). In what follows we will often omit the argument  $s$  in  $Q_{\mu}$  for brevity.

The properties of the system’s noise are determined by the noise spectral density  $S(\omega)$

$$\int_0^{\infty} dt e^{i\omega t} \langle e^{iH_B t} Q_{\mu} e^{-iH_B t} Q_{\nu} \rangle = S(\omega) \delta_{\mu\nu}, \quad (17)$$

where the inclusion of the Kronecker delta function  $\delta_{\mu\nu}$  is a consequence of the assumption of independent baths.

The effect of the noise on multiqubit quantum annealing was studied numerically in [49] in the case of Ohmic spectral density [50]

$$S_{\text{Ohmic}}(\omega) = \hbar^2 \frac{\eta \omega \exp(-\omega \tau_c)}{1 - \exp(-\hbar \omega / k_B T)}, \quad (18)$$

where  $\eta$  is the Ohmic damping coefficient and  $\omega_c = 1/\tau_c$  is a high-frequency cutoff. That work assumed weak system-environment coupling and utilized the Redfield formalism to derive the quantum Markovian master equation in the basis of the (instantaneous) adiabatic eigenstates of the qubit Hamiltonian. It was built on earlier studies of open-system quantum annealing where similar assumptions were made [51–55].

In addition to Ohmic noise, an important role is played by a low-frequency noise of the  $1/f$  type [56, 57] produced by the spins in the amorphous parts of the qubit device [26, 28, 58]. In current D-Wave chips this noise is coupled to the flux qubit relatively strongly as was shown in recent experiments [31]. Additionally, our analysis shows that noise effects are significantly enhanced by collective effects associated with multiqubit tunneling. While future generations of quantum annealer chips will hopefully have reduced levels of flux qubit noise, it will still produce a highly nonlinear effect for sufficiently large number of tunneling qubits.

In recent years, the noise spectrum of flux qubits was studied using a variety of approaches that includes dynamical decoupling schemes [59], free-induction Ramsey interference [60], coherent spectroscopy with strong microwave driving [61], and macroscopic resonant tunneling (MRT) techniques [31, 62].

In MRT experiments performed on the D-Wave One chip the qubit state is probed in a way that is most similar (compared with other methods) to the quantum annealing process itself, with no use of high-frequency drive and with just slow tunneling for each qubit within its group-state manifold. While the exact microscopic models of low-frequency noise are not well understood [26, 28] its effect on the system evolution in MRT experiments appeared to be well-described by phenomenological models [31, 62]. There, the quantity of interest is the incoherent-tunneling rate between the “up” and “down” eigenstates of the single flux qubit Hamiltonian  $-\frac{1}{2}(\epsilon_1\sigma^z + \Delta_1\sigma^x)$  as a function of the bias  $\epsilon_1$ . In [63], the Gaussian form of the MRT line is described with a noise model whose spectral density is sharply peaked at low frequency. In [31], this model is extended by attributing the linear form of the tails in the MRT line shape to the high-frequency (Ohmic) part of the noise spectral density. The MRT data collected for small tunneling amplitudes ( $\Delta_1/(2\pi\hbar) < 1$  MHz) and in a broad range of biases (0.4 MHz–4 GHz) and temperatures (21 mK – 38 mK) is surprisingly well-described by a phenomenological “hybrid” noise model

$$S(\omega) = S_{\text{If}}(\omega) + S_{\text{Ohmic}}(\omega), \quad (19)$$

where the high-frequency part of the spectral density has Ohmic form (18) and the low-frequency part  $S_{\text{If}}(\omega)$  is described only by the two parameters related to the width  $W$  and shift  $\epsilon_p$  of the MRT line [63]:

$$W^2 = \int_{-\infty}^{\infty} \frac{d\omega}{2\pi} \frac{S_{\text{If}}(\omega)}{\hbar^2}, \quad (20)$$

$$\epsilon_p = \int_{-\infty}^{\infty} \frac{d\omega}{2\pi} \frac{S_{\text{If}}(\omega)}{\hbar^2} \frac{1}{\omega(1 + \coth(\hbar\omega/(2k_B T)))}. \quad (21)$$

These parameters are also well known in physics in the context of the Pekar-Huang-Rhys theory [64, 65] of phonon broadening of the electron optical transitions in impurity centers in solids. The shift  $\epsilon_p$  is often called the reorganization energy, i.e. the energy change of the bath degrees of freedom during an incoherent tunneling process (it is conventionally called a Stokes shift in the theory of optical transitions). The

width  $W$  and shift  $\epsilon_p$  measured in [31] satisfy with high accuracy the thermodynamic relation

$$\epsilon_p = \frac{\hbar W^2}{2k_B T}. \quad (22)$$

This requires that the integrals in Eqs. (20) and (21) are dominated by the range of frequencies  $\omega \lesssim \omega_{\text{If}} \ll k_B T/\hbar$  where  $\omega_{\text{If}}$  is a characteristic cutoff of the low-frequency noise. The above hybrid model uses no information about the noise spectrum at frequencies below  $W$  except the assumption that  $\omega_{\text{If}} \ll W$  which is well justified because in the experiments  $\hbar W$  is of the same order as  $k_B T$  [31].

The hybrid noise model parameters were measured on D-Wave One [31] and D-Wave Two chips near the end of the quantum annealing schedule,  $s \simeq 1$ . The values of the noise parameters at a point during the annealing can be related to the measured ones (see App. A 5)

$$\frac{\eta(s)}{\eta_{\text{MRT}}} = \left( \frac{W(s)}{W_{\text{MRT}}} \right)^2 = \frac{B(s)}{B(1)} \quad (23)$$

$$W_{\text{MRT}}/(2\pi\hbar) = 0.4 \text{ GHz}, \quad \eta_{\text{MRT}} = 0.24 \quad (24)$$

where the above values correspond to the measurements done with the D-Wave Two chip.

## B. Three stages of quantum annealing process

During quantum annealing the system follows several stages depending on the magnitude of the instantaneous energy gap between the two lowest energy eigenstates of the control Hamiltonian  $H_0(s)$ . The instantaneous energy spectrum is

$$H_0(s)|\psi_\gamma(s)\rangle = E_\gamma(s)|\psi_\gamma(s)\rangle. \quad (25)$$

At the beginning of quantum annealing, the qubit Hamiltonian  $H_0$  is dominated by the driver Hamiltonian term  $H^D$  and the energy gap between the ground state and the first excited state ( $2A(s) \sim 5$  GHz) is very large compared to the temperature. At that stage the system resides in a ground state  $|\psi_0(s)\rangle$  with overwhelming probability.

In our case the evolution of the system beyond the initial *gapped* phase is significantly different from the case of low connectivity systems such as the linear chain considered in [49]. Because the dominant interaction in the problem Hamiltonian  $H^P$  is intra-cell ferromagnetic coupling with high degree of qubit connectivity the system dynamics during quantum annealing is well described as an evolution of the coupled large spins (spin value  $n/2$ ) corresponding to the two ferromagnetic clusters. The flipping of individual spins in each unit cell rises the energy by a large amount and therefore, when  $h_1$  is close to  $J/2$ , the system evolution is well-described by the two lowest energy eigenstates that corresponds to the clusters moving as a whole.

For local fields  $h_1 < J/2$ , the system evolution goes through the so-called “avoided-crossing” region

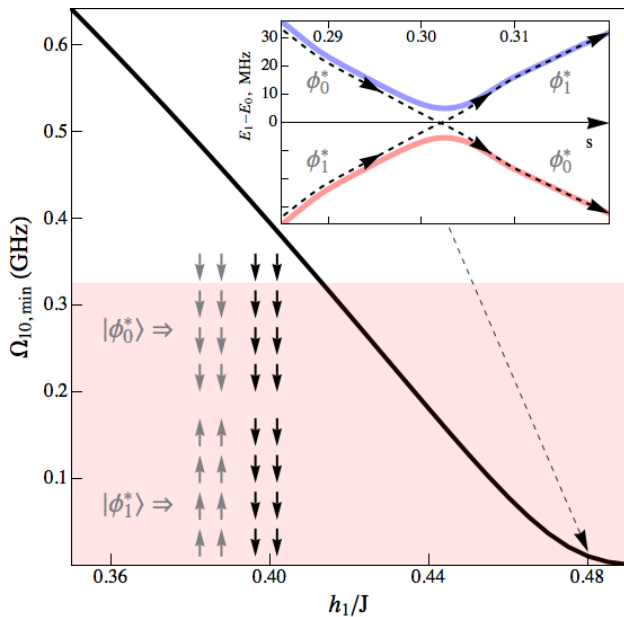


FIG. 7. The minimum gap between the ground- and first excited-state levels  $\Omega_{10,\min} = \min_{s \in (0,1)} [E_1(s) - E_0(s)]/\hbar$  (25) during quantum annealing as a function of the rescaled bias  $h_1/J$  is shown by the solid green line. The horizontal boundary of the red-filled area at 324MHz corresponds to 15.5mK, which is the lowest temperature in our experiments. The bias value  $h_1/J = 0.5$  corresponds to zero energy gap, achieved at the end of quantum annealing when the eigenstates of  $H_0(t_{qa}) = H_P$  with parallel and anti-parallel cluster orientations are degenerate. The upper inset shows the avoided crossing between the energy levels  $\{E_1(s), E_0(s)\}$  in the weak-strong cluster problem at  $h_1/J = 0.48$ . Dashed lines show the energy levels corresponding to the diabatic basis of states  $\{|\phi_1^*(s)\rangle, |\phi_0^*(s)\rangle\}$  (33) formed by the rotation of the adiabatic eigenstates (25) that maximizes the average Hamming distance (29), (32) between the spin configurations. The lower inset shows the spin configurations in both clusters that dominate the characteristics of the eigenstates before and after the avoided crossing. While transversing the avoided crossing, spins in the left cluster (shown in grey) reverse their orientations.

at intermediate times where the two lowest eigenstates  $E_1(s)$  and  $E_0(s)$  approach closely to, and then repel from, each other (see inset in Fig. 7). This level repulsion occurs due to the collective tunneling of qubits in the left cluster between the opposite  $z$ -polarizations. At the point where the gap  $\hbar\Omega_{10}(s) = E_1(s) - E_0(s)$  reaches its minimum the adiabatic eigenstates  $\{|\psi_0\rangle, |\psi_1\rangle\}$  are formed by the, respectively, symmetric and anti-symmetric superpositions of the cluster orientations.

In the minimum gap region the coupling of the qubit system to the environment causes fast transitions between the states giving rise to thermalization. Unlike the case of quantum annealing in a linear qubit chain [49] only the two lowest levels will be thermalized with the rest of the levels being unoccupied because the energy splitting at the avoided crossing obeys  $\hbar\Omega_{10} \lesssim k_B T$  and is much smaller than the separation to the next energy level (which is in excess of 3GHz, see Fig. 3).

After the avoided-crossing region the ground state  $|\psi_0(s)\rangle$  and first excited state  $|\psi_1(s)\rangle$  gradually evolve into product states with the same and opposite cluster orientations, respectively. There the evolution of the system is dominated by the spontaneous symmetry breaking signature of the quantum phase transition: a steep increase of the  $z$ -magnetizations of the clusters (see Fig. 5). The transitions between the states  $|\psi_0(s)\rangle$  and  $|\psi_1(s)\rangle$  involve progressively larger numbers of tunneling qubits leading to an exponential slow-down of the transitions as shown in Fig. 11 (see also Fig. 8).

The *slowdown* phase of quantum annealing is followed by the *frozen* phase where the transition rates are much slower than the quantum annealing rate so that the population of the levels do not change during this phase. Part of the system population remains trapped in the excited state  $|\psi_1(s)\rangle$  until the end of the quantum annealing process. The success probability of quantum annealing is (roughly) determined by the Boltzmann factor for the relative thermal populations of the first two states during the slow-down phase.

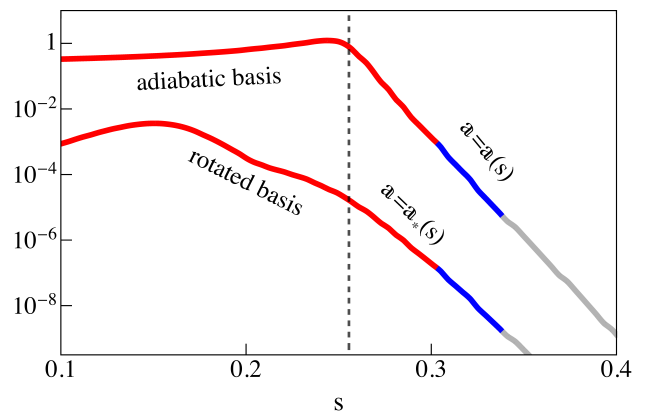


FIG. 8. Dependence of the transition matrix element coefficient  $\alpha$  on  $s$  for  $h_1 = 0.44J$ . The two plots correspond to the coefficient in the adiabatic basis  $\{|\psi_0\rangle, |\psi_1\rangle\}$  and rotated basis (see (33)) of the pointer states. Vertical dashed line indicates the point where the minimum energy gap is reached (avoided-crossing). Red, blue, and gray colors indicate the different stages of quantum annealing (thermalization, slowdown, frozen) described in the text. The boundary between the thermalized and slowdown phases corresponds to  $\Gamma_{1 \rightarrow 0} t_{qa} = 10$ . The boundary between the slowdown and frozen phases corresponds to  $\Gamma_{1 \rightarrow 0} t_{qa} = 0.1$

In the analysis of the transitions between the states we start from the initial (gapped) stage when the instantaneous energy gap  $\hbar\Omega_{10}(s) = E_1(s) - E_0(s)$  is sufficiently large compared to  $\hbar W(s)$  (see Fig. 11) and the coupling to the environment can be treated as a perturbation. Then the transition rate from the first excited state to the ground state is given by Fermi's golden rule for a single-boson process:

$$\Gamma_{1 \rightarrow 0}^{FGR}(s) = \frac{\alpha(s)}{\hbar^2} S(\Omega_{10}(s)), \quad (26)$$



where

$$\mathfrak{a}(s) = \frac{1}{4} \sum_{\mu=1}^{2n} |Z_{\mu}^{10}(s)|^2. \quad (27)$$

Here and below we use the following notation for the matrix elements:

$$Z_{\mu}^{\gamma\gamma'}(s) = \langle \psi_{\gamma}(s) | \sigma_{\mu}^z | \psi_{\gamma'}(s) \rangle, \quad \gamma, \gamma' = \{0, 1\}. \quad (28)$$

This is an overlap factor that determines how strongly the transition  $1 \leftrightarrow 0$  is coupled to the environment.

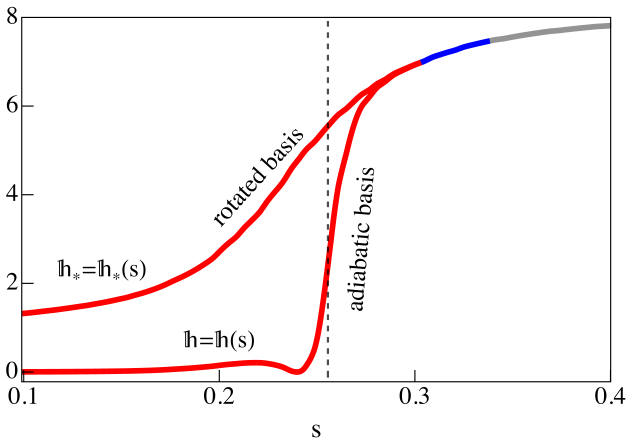


FIG. 9. Dependence of the average Hamming distance between the two lowest-energy eigenstates on  $s$  for the adiabatic basis  $\{|\psi_0\rangle, |\psi_1\rangle\}$  and the rotated diabatic basis (33) for  $h_1 = 0.44J$ . The vertical dashed line indicates the point where the minimum energy gap is reached (avoided-crossing). Red, blue, and gray colors indicate the different stages of quantum annealing described in the text. The boundary between the thermalized and slowdown phases corresponds to  $\Gamma_{1 \rightarrow 0} t_{qa} = 10$ . The boundary between the slowdown and frozen phases corresponds to  $\Gamma_{1 \rightarrow 0} t_{qa} = 0.1$

Fig. 8 shows the dependence of  $\mathfrak{a}(s)$  on the annealing parameter  $s$ . We observe a steep exponential fall-off of this coefficient after the avoided crossing. This happens because, in accord with the discussion above, starting from the avoided crossing region, intra-cell ferromagnetic interaction plays a substantial role by causing the spins in each unit cell to move *in unison*, forming two clusters with total spin value  $n/2$  each. As can be seen from Fig. 5, *after* the avoided crossing the first two eigenstates  $|\psi_0\rangle$  and  $|\psi_1\rangle$  correspond to opposite total spin  $z$ -projections of the left cluster. When  $s$  increases, the average “Hamming distance” between the eigenstates,

$$h(s) = \frac{1}{4} \sum_{\mu=1}^{2n} |Z_{\mu}^{11}(s) - Z_{\mu}^{00}(s)|^2, \quad (29)$$

also increases very steeply as shown in Fig. 9. (We note that the maximum value of  $h(s)$  is proportional to  $n$ .) In that region the transition between the eigenstates requires multiqubit tunneling of a progressively higher order, leading to an exponential decay of the overlap coefficient  $\mathfrak{a}(s)$  with  $s$  and a steep deceleration of the environment-induced transitions between

the two states, as can be seen from the plot of  $\Gamma_{1 \rightarrow 0}(s)$  in Fig. 11.

The fact that qubits within each unit cell tend to move together, forming large spins, amplifies the effect of the environment on their quantum dynamics. In particular, we will show below that the effective linewidth of the low-frequency noise as seen by the two-state system  $\{|\psi_1(s)\rangle, |\psi_0(s)\rangle\}$  is  $h^{1/2}(s)W(s)$  and that the effective Ohmic coefficient is  $h(s)\eta(s)$ . This amplification becomes important at the slowdown stage of quantum annealing when clusters increase their  $z$ -polarizations and  $h \sim n \gg 1$  (see Fig. 11). For sufficiently large  $h^{1/2}(s)W(s) \gtrsim \Omega_{10}$ , the description of the system dynamics becomes substantially non-perturbative in the spin-boson interaction. Equilibria of the environmental degrees of freedom shift depending on the collective qubit-state, which in turn affects the state itself causing the *polaronic* effect. In this case, the adiabatic basis of instantaneous eigenstates  $\{|\psi_1(s)\rangle, |\psi_0(s)\rangle\}$  formed by the superposition of up and down cluster orientations loses its physical significance. Instead, the dynamics occurs between the two states  $\{|\phi_1(s)\rangle, |\phi_0(s)\rangle\}$  with the predominately opposite cluster orientations corresponding (roughly) to the bottoms of the wells of the classical potential separated by the barrier as shown in Fig. 4.

We introduce a unitary rotation on angle  $\vartheta$  defining the rotated basis of states  $|\phi_{\gamma}(\vartheta, s)\rangle$ :

$$|\phi_{\gamma}\rangle = \sum_{\gamma'=0,1} (-1)^{\gamma\gamma'+\gamma'+1} \cos\left(\frac{\vartheta}{2} - (-1)^{\gamma+\gamma'} \frac{\pi}{4}\right) |\psi_{\gamma'}\rangle, \quad (30)$$

where  $\gamma, \gamma' = \{0, 1\}$ . The corresponding matrix elements are

$$Z_{\mu}^{\gamma\gamma'}(\vartheta, s) = \langle \phi_{\gamma}(\vartheta, s) | \sigma_{\mu}^z | \phi_{\gamma'}(\vartheta, s) \rangle, \quad \gamma, \gamma' = 0, 1. \quad (31)$$

We find the angle  $\vartheta_*(s)$  that maximizes the average Hamming distance between the states

$$h_*(s) = \max_{\vartheta} \frac{1}{4} \sum_{\mu=1}^{2n} |Z_{\mu}^{11}(\vartheta, s) - Z_{\mu}^{00}(\vartheta, s)|^2. \quad (32)$$

Then our new instantaneous basis will be defined as

$$|\phi_{\gamma_*}(s)\rangle = |\phi_{\gamma}(\vartheta_*(s), s)\rangle, \quad \gamma = \{0, 1\}. \quad (33)$$

The system dynamics is mainly a hopping process between these states associated with the incoherent tunneling of the spins in the left cluster connecting states with predominantly “up” ( $|\phi_{1*}\rangle$ ) and “down” ( $|\phi_{0*}\rangle$ ) qubit configurations. The Hamming distance between these states is  $h_*(s)$  (shown in Fig. 9). In fact the transition rate between the states in the rotated basis (to be computed below) is minimized for the angle of Eq. (32). In essence, this approach is related to the pointer basis idea, that the system tends to be localized in states induced by environmental coupling [66]. In what follows a subscript  $*$  will denote quantities computed in the rotated basis.

The rotation angle  $\vartheta_*(s)$  during the annealing is shown in Fig.10 for different values of  $h_1/J$ . In the

later stages of the annealing the angle  $\vartheta$  always approaches the value  $\pi/2$  that corresponds to the adiabatic (energy) basis with state  $|\phi_{1*}\rangle$  being an excited state (30). In other words, quantum annealing along the pointer states arrives at the encoded solution of the computational problem because, toward the end of the annealing, the rotated basis converges back to eigenstates of the problem Hamiltonian.

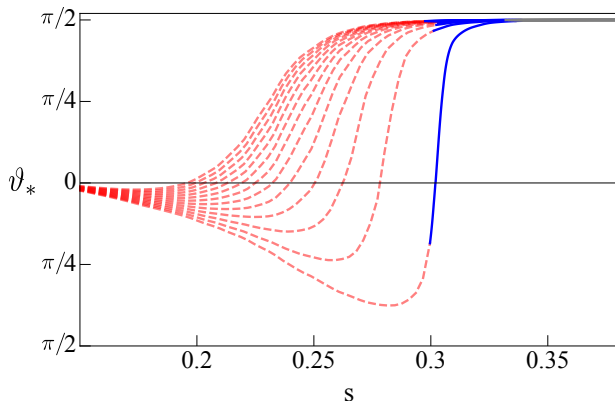


FIG. 10. Optimal rotation angles  $\vartheta_*$  vs.  $s$  for eigenstates in the basis of Eq. (33) at different values of  $h_1/J = 0.35 + 0.01\kappa$ , with  $\kappa = 1, 2, \dots, 13$  corresponding to the curves in the figure numbered from the bottom to the top. Red corresponds to the thermalization phase, blue corresponds to the loss of thermalization (slowdown phase), and black corresponds to the frozen phase described in the main text. The boundary between the thermalized and slowdown phases corresponds to  $\Gamma_{1\rightarrow 0}t_{qa} = 10$ . The boundary between the slowdown and frozen phases corresponds to  $\Gamma_{1\rightarrow 0}t_{qa} = 0.1$ . Optimal rotation angles only have physical meaning starting from about the end of the thermalization phase where the spins in the clusters start to behave in a concerted manner. All angles approach  $\pi/2$  in a frozen phase corresponding to the adiabatic eigenstates.

We will show below (cf. Eq. (64)) that the non-perturbative treatment of the effects of noise and dissipation does not change the Markovian nature of the system dynamics but modifies the instantaneous transition rate  $\Gamma_{1\rightarrow 0}(s)$  compared to its value  $\Gamma_{1\rightarrow 0}^{FGR}(s)$  given in Eq. (26) for a single-boson process. The non-perturbative analysis in the rotated basis is justified within the context of the theory of spin-boson interaction developed in [50]. The individual transitions due to the coupling to bosons are associated with so-called “blip-cojourn” pairs with blips forming a dilute gas if the duration of the blip  $\tau_b = 1/\hbar^{1/2}(s)W(s)$  is much shorter than the characteristic inter-blip distance  $\sim 1/\Gamma_{1\rightarrow 0}(s)$ , with

$$\Gamma_{1\rightarrow 0}(s) \ll \hbar^{1/2}(s)W(s). \quad (34)$$

In the adiabatic basis,  $\hbar(s)$  can reach very small values near the avoided crossing (see Fig.9) due to quantum superpositions. In the optimally rotated basis,  $\tau_b^{-1} = \hbar_*(s)^{1/2}W(s)$  is monotonically increasing during the annealing to its maximum value ( $n=8$  in the problem of interest). When the condition (34) is satisfied at the last stages of the annealing, the gas of blips is dilute and we can apply the Noninteracting-blip Approximation (NIBA) [50]. While this method

was developed to analyze a Landau-Zener problem in a driven spin-1/2 system coupled to a finite temperature bath in a number of papers [29, 30, 67], its application in the present context of strongly correlated qubit dynamics is novel and leads to qualitatively new features.

Before we proceed further with the NIBA analysis, we emphasize that our theory will not provide an accurate treatment of the region of  $s$  where  $\hbar^{1/2}(s)W(s) \sim \Gamma_{1\rightarrow 0}$ , representing a crossover between the perturbative treatment based on single-boson processes and Ohmic spectral density (with  $\Gamma_{1\rightarrow 0}^{FGR}(s)$  given in Eq. (26)) and non-perturbative NIBA theory that includes low-frequency noise. In this intermediate region the low-frequency noise cannot be described just by the two characteristics of its spectral density treated here (cf. Eqs. (21) and (20)) and we are simply lacking the experimental data for the theoretical analysis.

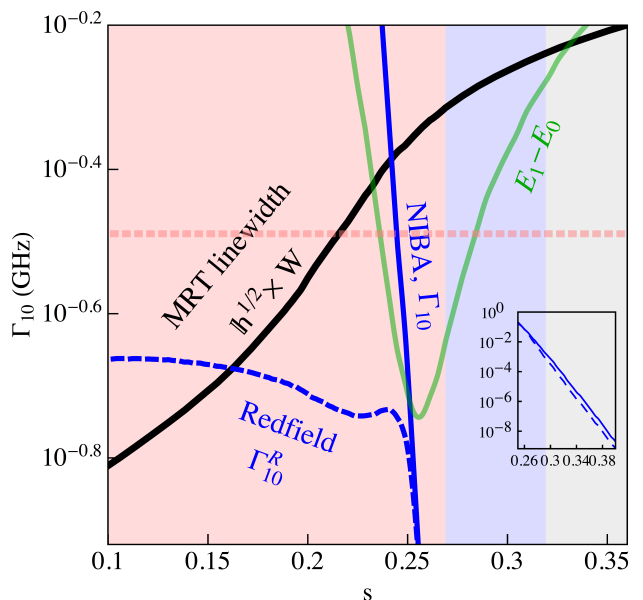


FIG. 11. The solid black line shows the dependence of the effective MRT linewidth of the low-frequency noise  $\hbar^{1/2}(s)W(s)/(2\pi)$  (GHz) on annealing parameter  $s$ . The dashed blue line is a plot of the single boson transition rate  $\Gamma_{1\rightarrow 0}^{FGR}$  vs.  $s$  calculated using Fermi’s golden rule, Eq. (26), with Ohmic spectral density. The solid blue is a plot of the transition rate  $\Gamma_{1\rightarrow 0}$  calculated using the NIBA equation (66). The green line shows the  $s$ -dependence of the energy gap  $(E_1(s) - E_0(s))/(2\pi\hbar)$  between the two lowest-energy levels during the annealing at 15.5 mK. The lowest temperature in our experiments is shown by the horizontal red dotted line. All plots correspond to bias  $h_1 = 0.44J$ . At the early stage of quantum annealing  $\hbar^{1/2}(s)W(s) \ll (E_1(s) - E_0(s))/\hbar$  and  $\Gamma_{1\rightarrow 0}^{FGR}$  gives an accurate description of the dynamics. Red, blue and gray filling areas correspond to the phases of quantum annealing (respectively, thermalization, slowdown and frozen) described in the main text. The boundary between the thermalized and slowdown phases corresponds to  $\Gamma_{1\rightarrow 0}t_{qa} = 10$ . The boundary between the slowdown and frozen phases corresponds to  $\Gamma_{1\rightarrow 0}t_{qa} = 0.1$ . The inset shows the transition rates  $\Gamma_{1\rightarrow 0}^{FGR}$ ,  $\Gamma_{1\rightarrow 0}$  vs.  $s$  for a greater range of values. One can see that even at the end of the thermalization phase  $\hbar^{1/2}(s)W(s) \gg \Gamma_{1\rightarrow 0}$ , justifying the NIBA approximation discussed in the main text.

Our main observation is that this region does not affect the population of the ground state at the end of quantum annealing. Since the quantum annealing rate  $1/t_{qa}=50$  kHz is constant, the system stays very close to instantaneous thermal equilibrium while

$$\Gamma_{1\rightarrow 0}(s) \gg 1/t_{qa} \quad (35)$$

(see Fig. 11). This is a “thermalization phase” of the annealing process. On the other hand, due to the strong effect of low-frequency noise on D-Wave qubits the condition

$$1/t_{qa} \ll \hbar^{1/2}(s)W(s) \quad (36)$$

is held almost everywhere except for the very early stages (cf. Fig. 11). Therefore the non-perturbative regime of condition (34) is established well within the thermalization phase where the (Gibbs) distribution is not sensitive to the noise model.

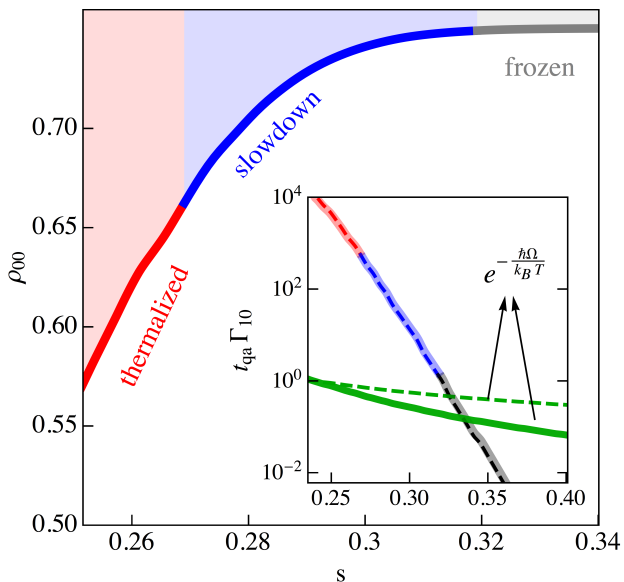


FIG. 12. Main plot shows the evolution of the population of the pointer state  $\rho_{00} = \langle \phi_0^*(s) | \rho | \phi_0^*(s) \rangle$  as a function of the annealing parameter  $s$ . Red, blue and gray filling areas correspond to the phases of quantum annealing (respectively, thermalization, slowdown and frozen) described in the text. The boundary between the thermalized and slowdown phases corresponds to  $\Gamma_{1\rightarrow 0} t_{qa} = 10$ . The boundary between the slowdown and frozen phases corresponds to  $\Gamma_{1\rightarrow 0} t_{qa} = 0.1$ . In the inset the solid line shows the dependence of  $t_{qa} \Gamma_{1\rightarrow 0}$  (66) on the annealing parameter  $s$ . Different color portions correspond to the same annealing phases as in the main plot. The solid green line is a plot of the Boltzmann factor for the instantaneous energy difference  $\hbar\Omega(s)$  between the pointer states given in (43). Both lines are plotted at 15.5 mK. Dashed lines correspond to the temperature 35 mK. All data are for the value of the local field  $h_1/J = 0.44$ .

At a later stage the thermal distribution can no longer be supported due to the steep slowdown of the transition rates as shown in Fig. (12). Eventually the system enters the final “frozen” stage where the transitions are suppressed over the period of the annealing and part of the system population remains trapped in the excited state. As can be seen in the Fig. 12,

the success probability is determined by the occupation of the ground state at the beginning of the frozen phase. This, in turn, is given by the thermal equilibrium population  $\frac{1}{2}(1 + \tanh(\hbar\Omega(s)/2k_B T))$  where  $\hbar\Omega(s)$  is the difference of the energies of the pointer states  $|\phi_{1*}\rangle$  and  $|\phi_{0*}\rangle$ , as given in Eq. (43). When the temperature grows, the transition rates dominated by low-frequency noise change very little in the studied temperature range, while the thermal population decreases appreciably. This reduces the success of quantum annealing, as will be seen later, and is the origin of the observed thermal reduction.

### C. Non Interacting Blip Approximation

To implement NIBA in our problem we need to explicitly represent the boson operators for normal modes of the environmental free-boson Hamiltonian

$$H_B = \sum_{\mu=1}^{2n} \sum_u \hbar\omega_{\mu u} (b_{\mu u}^\dagger b_{\mu u} + 1/2) \quad (37)$$

$$Q_\mu = \sum_u \lambda_{\mu u} (b_{\mu u}^\dagger + b_{\mu u}), \quad \mu = 1, \dots, 2n. \quad (38)$$

Here  $\mu$  indexes qubits,  $u$  indexes the bath modes, and  $\lambda_{\mu u}$  and  $\omega_{\mu u}$  are the microscopic parameters that will not enter into any observable directly but will do so only via the spectral function of Eq. (19), which takes the form

$$S(\omega, s) = \frac{2\pi \sum_u \lambda_{\mu u}^2 \delta(\omega - \omega_{\mu u})}{1 - \exp(-\hbar\omega/k_B T)}$$

identical for each qubit. We explicitly note that  $S \equiv S(\omega, s)$  depends on the quantum annealing parameter  $s$  (see Eqs. (23) and (24) as well as Sec. A). We proceed by making a small polaron transformation of the original Hamiltonian with unitary operator

$$U(s) = \exp \left[ \sum_\gamma -\Lambda_\gamma(s) |\phi_{\gamma*}(s)\rangle \langle \phi_{\gamma*}(s)| \right].$$

Here we use the notation

$$\Lambda_\gamma(s) = \sum_{\mu u} \xi_{\mu u}^{\gamma\gamma}(s) (b_{\mu u} - b_{\mu u}^\dagger), \quad (39)$$

$$\xi_{\mu u}^{\gamma\gamma'}(s) = \frac{\lambda_{\mu u}}{\hbar\omega_{\mu u}} Z_{\mu*}^{\gamma\gamma'}(s),$$

where  $\gamma \in \{0, 1\}$  and the matrix elements  $Z_{\mu*}^{\gamma\gamma'}$  are defined in the basis of optimally rotated states as

$$Z_{\mu*}^{\gamma\gamma'}(s) = \langle \phi_{\gamma*}(s) | \sigma_\mu^z | \phi_{\gamma'*}(s) \rangle. \quad (40)$$

The system-bath Hamiltonian (16) after the polaron transformation  $\mathbb{H} = U H U^{-1}$  is

$$\mathbb{H}(s) = \mathbb{H}_0(s) + \mathbb{H}_{\text{int}}(s) + H_B \quad (41)$$

where

$$\mathbb{H}_0(s) = \hbar\Omega(s) (|\phi_{1*}(s)\rangle \langle \phi_{1*}(s)| - |\phi_{0*}(s)\rangle \langle \phi_{0*}(s)|), \quad (42)$$

$$\Omega(s) = \Omega_{10}^*(s) - \epsilon_p(s)\mathfrak{d}_*(s), \quad (43)$$

$$\Omega_{10}^*(s) = \Omega_{10}(s) \sin \vartheta_*(s) \quad (44)$$

and  $\Omega_{10}(s) = (E_1(s) - E_0(s))/\hbar$ . Here  $\Omega_{10}^*(s)$  corresponds to the system energy gap in a rotated basis and the second term gives the polaronic shift due to the reorganization energy of the environment. Similar

to the linewidth, it is renormalized with respect to its single qubit MRT value by a coefficient  $\mathfrak{d}_*(s)$  reflective of a collective qubit behavior:

$$\mathfrak{d}_*(s) = \frac{1}{4} \sum_{\mu=1}^{2n} [(Z_{\mu*}^{11})^2(s) - (Z_{\mu*}^{00})^2(s)]. \quad (45)$$

The Hamiltonian  $\mathbb{H}_{\text{int}}(s)$  is strictly non-diagonal in the rotated basis and explicitly involves boson operators

$$\mathbb{H}_{\text{int}}^{\gamma\gamma'}(s) = \left( \frac{\hbar\Delta_*(s)}{2} + \sum_{\mu,u} Z_{\mu*}^{\gamma\gamma'}(s) \lambda_{\mu u} (b_{\mu u}^\dagger + b_{\mu u} - 2\xi_{\mu u*}^{\gamma\gamma'}(s)) \right) e^{\Lambda_{\gamma'\gamma}(s)}, \quad (46)$$

where  $\Lambda_{\gamma'\gamma} = \Lambda_{\gamma'} - \Lambda_{\gamma}$  and  $\Delta_*$  represent off-diagonal elements of the system Hamiltonian in the rotated basis

$$\Delta_*(s) = -\Omega_{10}(s) \cos \vartheta_*(s). \quad (47)$$

While the original NIBA calculation [50] was quite involved, a very simple prescription for how to apply it was given in [68], which we will follow below. We start from the quantum Liouville equation for the full

system-bath density operator  $\varrho(s)$ :

$$i\hbar \frac{d\varrho}{dt} = [\mathbb{H}_0(s(t)) + \bar{\mathbb{H}}_{\text{int}}(s(t), t), \varrho(t)], \quad (48)$$

where we employed the interaction picture for bosons

$$\bar{\mathbb{H}}_{\text{int}}(s, t) = \exp(iH_B t/\hbar) \mathbb{H}_{\text{int}}(s) \exp(-iH_B t/\hbar). \quad (49)$$

We write the density matrix in the rotated basis  $\{|\phi_{\gamma*}\rangle\}$  and express its non-diagonal matrix elements through the diagonal ones as

$$\varrho_{10}(t) = \varrho_{10}(0) + \frac{1}{i\hbar} \int_0^t d\tau e^{\frac{i}{\hbar} \int_\tau^t d\tau' \Omega(s(\tau'))} [\bar{\mathbb{H}}_{\text{int}}^{10}(s(\tau), \tau) \varrho_{00}(\tau) - \varrho_{11}(\tau) \bar{\mathbb{H}}_{\text{int}}^{10}(s(\tau), \tau)], \quad (50)$$

where  $s(t) = t/t_{qa}$  is the quantum annealing parameter. Next we use the fact that the initial state for quantum annealing corresponds to  $\varrho_{10}(0) = 0$ . We

then plug the non-diagonal matrix elements from (50) back into (48) and obtain the equations for the diagonal matrix element

$$\frac{d\varrho_{11}}{dt} = -\frac{1}{\hbar^2} \int_0^t d\tau e^{\frac{i}{\hbar} \int_\tau^t d\tau' \Omega(s(\tau'))} [\bar{\mathbb{H}}_{\text{int}}^{10}(s(t), t) \bar{\mathbb{H}}_{\text{int}}^{01}(s(\tau), \tau) \varrho_{11}(\tau) - \bar{\mathbb{H}}_{\text{int}}^{10}(s(t), t) \varrho_{00}(\tau) \bar{\mathbb{H}}_{\text{int}}^{01}(s(\tau), \tau)] + \text{h.c.} \quad (51)$$

and a similar equation for  $\varrho_{00}$ . Here we neglected the basis dragging terms of the type  $\langle \phi_1(s) | \dot{\phi}_0(s) \rangle$ , because we focus on the situation where Landau-Zener transitions are negligible ( $t_{qa} \Omega_{10}^{\text{min}} \gg 1$ ). Other than that the expression above is *exact*.

We introduce an approximation and insert the free-bath dynamics into the expressions for  $H_{\text{int}}^{\gamma\gamma'}(t)$  by replacing time-dependent boson operators  $b_{\mu u}(t)$  with  $b_{\mu u}(t) e^{-i\omega_{\mu u} t}$ . We then introduce the decoupling ansatz for the full density matrix:  $\varrho = \rho \otimes \rho_B$ , where  $\rho_B$  is the Gibbs density operator for the bath and  $\rho = \text{Tr}_B[\varrho]$  is the reduced density matrix of the qubit system. We then average Eq. (51) with respect to the

bath, which can be done in a tedious but straightforward manner since averaging involves only free-boson operators. We write the resulting equation of the difference in populations of the rotated (pointer) states  $z(t) = \rho_{11}(t) - \rho_{00}(t)$  as

$$\frac{dz(t)}{dt} = \int_0^t dt' h(t-t', s(t)) - z(t) \int_0^t dt' g(t-t', s(t)), \quad (52)$$

where the functions  $h$  and  $g$  are given below. In the above equation we removed the time delay for the population difference by replacing  $z(t-t')$  with  $z(t)$ . This is possible to do because the time scale for its variation (inverse transition rates  $1/\Gamma_{1\rightarrow 0}$ ) is assumed to

be much longer than the correlation time of the environment  $\tau_b$  (see equation (34) and discussion there). The precise condition for this will be discussed later. In Eq. (52) we also neglected the variation of the annealing parameter  $s(t')$  over the range of integration  $t - t'$  because  $t_{qa} \gg \tau_b$  (see Eq. (36)).

The functions  $h$  and  $g$  used in (52) are

$$h(\tau, s) = 2Re[e^{i\Omega(s)\tau}(C_{01}^*(\tau, s) - C_{10}(\tau, s))] \quad (53)$$

$$g(\tau, s) = 2Re[e^{i\Omega(s)\tau}(C_{01}^*(\tau, s) + C_{10}(\tau, s))], \quad (54)$$

where

$$C_{\gamma\gamma'}(\tau, s) = \frac{1}{\hbar^2} Tr \left[ \rho_B \bar{\Gamma}_{\text{int}}^{\gamma\gamma'}(s, \tau) \bar{\Gamma}_{\text{int}}^{\gamma'\gamma}(s, 0) \right] \quad (55)$$

One can show that  $C_{\gamma\gamma'}(\tau, s)$  satisfies the Kubo-Martin-Schwinger (KMS) condition

$$C_{\gamma\gamma'}(t) = C_{\gamma'\gamma}(-t - i\beta) \quad (56)$$

as well as

$$C_{\gamma\gamma'}^*(t) = C_{\gamma\gamma'}(-t). \quad (57)$$

These conditions ensure that for a fixed  $s(t) = \text{const}$  the stationary solution for  $\rho_{\gamma\gamma}(t)$  is a thermal equilibrium distribution at temperature  $T = \hbar/(k_B\beta)$ .

The explicit form of  $C_{\gamma\gamma'}(\tau, s)$  is the central result of our analysis as it is distinct from the conventional NIBA theory (cf. Eqs. (7.5),(7.6) in [50]). It has the following form

$$C_{10}(\tau, s) = F_*(\tau, s) e^{-\hbar_*(s)f(\tau, s)}, \quad (58)$$

where

$$F_*(\tau, s) = \alpha_*(s) f_{\tau\tau}(\tau, s) + (\epsilon_p \mathfrak{c}_+^*(s) - i\mathfrak{c}_-^*(s) f_\tau(\tau, s) - \Delta_*(s)/2)^2. \quad (59)$$

Here, the off-diagonal matrix element  $\Delta_*(s)$  is given in (47) and we denoted  $f_{\tau\tau} = \partial^2 f / \partial \tau^2$ . We also used the average Hamming distance (32) and the transition matrix element coefficient  $\alpha(s)$  in Eq. (27) calculated in the rotated basis using matrix elements from Eq. (40). The function  $f(\tau, s)$  is related to the spectral density  $S(s, \omega)$  and appears in the context of the MRT theory of flux qubits [31, 63] and Marcus theory [69]:

$$f(\tau, s) = \int_{-\infty}^{\infty} \frac{d\omega}{2\pi} S(\omega, s) \frac{1 - e^{-i\omega\tau}}{(\hbar\omega)^2}. \quad (60)$$

The coefficients  $\mathfrak{c}_\pm^*(s)$  are defined in the optimally rotated (pointer basis)

$$\mathfrak{c}_\pm^*(s) = \frac{1}{4} \sum_{\mu=1}^{2n} Z_{\mu*}^{10}(s) (Z_{\mu*}^{11}(s) \pm Z_{\mu*}^{00}(s)), \quad (61)$$

where the matrix elements  $Z_{\mu*}^{\gamma\gamma'}$  are given in Eq. (40). Using the hybrid model of noise in Eq. (19) introduced in [31] the function  $f(\tau, s)$  takes the form

$$f(\tau, s) = i\epsilon_p(s)\tau + \frac{1}{2}W^2(s)\tau^2 - \frac{\eta}{2\pi} \ln G(\tau). \quad (62)$$

Here the function  $G(\tau)$  is closely related to the well-known functions  $Q_1(\tau), Q_2(\tau)$  discussed in Ref. [50] for the case of an Ohmic environment. Its explicit form is

$$G(\tau) = e^{-i \tan^{-1}(\tau\omega_c)} \sqrt{1 + (\omega_c\tau)^2} \frac{\Gamma((1 - i\tau\omega_c)/\beta\omega_c) \Gamma((1 + i\tau\omega_c)/\beta\omega_c)}{\Gamma^2(1/\beta\omega_c)} \quad (63)$$

where  $\Gamma(x)$  is the Gamma function. We note that in the range of parameters relevant to the present discussion one can treat  $1/\omega_c$  as a positive infinitesimally-small quantity that serves to regularize the integral in (52) and whose exact value does not enter the final result.

It follows from (58) and (60) that the functions  $g(\tau, s)$  and  $h(\tau, s)$  decay exponentially with  $\tau$  on the scale  $\tau_b = 1/(\hbar^{1/2}W(s))$  in correspondence with the discussion above (cf. (58) and (62)). The equation (52) can be re-written as follows:

$$\frac{dz}{dt} = -\Gamma(s)(z - \tan(\beta\Omega(s)/2)), \quad (64)$$

where  $s = t/t_{qa}$  and

$$\Gamma(s) = \Gamma_{0 \rightarrow 1} + \Gamma_{1 \rightarrow 0}, \quad \Gamma_{0 \rightarrow 1} = \Gamma_{1 \rightarrow 0} e^{-\beta\epsilon(s)}. \quad (65)$$

Here

$$\Gamma_{1 \rightarrow 0}(s) = 2Re \int_0^\infty d\tau e^{i\Omega(s)\tau - \hbar_*(s)f(\tau, s)} F_*(\tau, s), \quad (66)$$

where the function  $f$  is given in (60) and (62) and the function  $F$  is given in (59) and (61). The above equation can be simplified by making use of the condition that the temperature is much smaller than the cutoff frequency for Ohmic noise

$$\beta\omega_c \gg 1. \quad (67)$$

Expanding the Gamma functions in Eq. (63) we get

$$\Gamma_{1 \rightarrow 0}(s) = \int_{-\infty}^{\infty} d\tau e^{i(\Omega_{i0}^* - (\hbar_* + d_*)\epsilon_p)\tau - \frac{1}{2}\hbar_* W^2 \tau^2} \left[ \frac{i\beta}{\pi\tau_c} \sinh \left( \frac{\tau - i\tau_c}{\beta/\pi} \right) \right]^{-\frac{\hbar_*\eta}{2\pi}} F_*(\tau, s), \quad (68)$$



where the expression for  $F_*$  is given in Eq. (59). This is a transition rate from the state 1 to 0 that appears in a rate equation (64) for the population difference. This is a central result of our NIBA theory analysis.

The precise condition for neglecting the time-delay for  $z(t)$  in (52) can be derived within the context of the Keldysh-Schwinger non-equilibrium diagrammatic technique with respect to spin boson interaction. This approach was utilized in a number of studies of Landau-Zener phenomena with dissipation [30, 67, 70]. In the limit of short noise correlation time  $\tau_b$  the *pairing-off theorem* [30] states that non-crossing and non-overlapping diagrams on double-path Keldysh contour provide a dominant contribution to the dynamics. This theorem is analogue to the theorem proven by Abrikosov and Gorkov in their theory of impurities in a metal [71] as was pointed out in [70]. It also precisely corresponds to non-interacting-clip approximation (NIBA) developed in Ref. [50], where the criterion for the validity of this approximation is given. In our case this criterion amounts to the condition

$$g_1(s) = 2Re \int_0^\infty d\tau \tau e^{i\Omega(s)\tau - \hbar_*(s)f(\tau,s)} F(\tau,s) \ll 1. \quad (69)$$

We note that the expressions (66) and (69) differ only by the presence of the  $\tau$  in the integrand. This condition corresponds to  $\Gamma_{1 \rightarrow 0} \tau_b \ll 1$  because  $\tau_b = 1/\hbar^{1/2}(s)W(s)$  is the size of the interval beyond which the integrand in (66) decays exponentially. As it was discussed in the previous section, we only need to inspect the condition (69) at the end of the thermalization region. For the sake of numerical investigation, we define this by the value of  $s \approx s_{eq}$  where the deviation of the system state from the instantaneous Gibbs distribution is 1%. We then compute  $g_1$  at various values of parameters with the results given in Fig. 13. It can be seen that  $g_1 \ll 1$  in the entire parameter range under study.

We note in passing that the choice of the optimal basis rotation angle  $\vartheta_*(s)$  could be done differently from that given in Eq. (32) that maximizes the Hamming distance between clusters. Instead, one can calculate the transition rate  $\Gamma_{1 \rightarrow 0} = \Gamma_{1 \rightarrow 0}(\vartheta, s)$  as a function of the angle of the basis rotation and choose the angle so that it minimizes the transition rate between the states. In fact the optional angle we obtained in this way is extremely close to that obtained by maximizing the Hamming distance.

We observe a very close correspondence between the results of the analysis with the NIBA Quantum Master Equation and the D-Wave data displayed in Fig. 14. This figure shows the probability of success versus  $h_1 = [0.3, \dots, 0.48]$ . Tunneling can only be present for  $h_1 < 0.5$  when there is an energy barrier between the local and global minimum (seen as a bifurcation in the semi-classical energy landscape analysis, see Fig 6). We emphasize that for NIBA (and Redfield) we do not have any parameter fitting. We use parameters obtained experimentally from MRT measurements on the device (see Eqs. (23) (24) (62) and App. A).

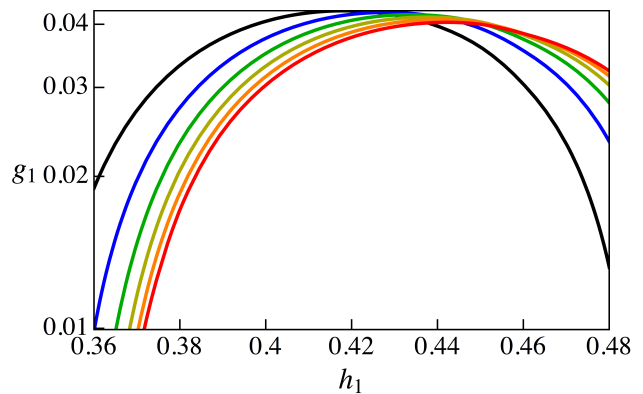


FIG. 13. Value of the coefficient  $g_1$  in the NIBA criterion (69) as a function of the local field  $h_1/J$  at different temperatures. Black, blue, green, yellow, orange, and red curves correspond to the temperature values of 15.5, 20, 25, 30, 35, and 40 mK, respectively.

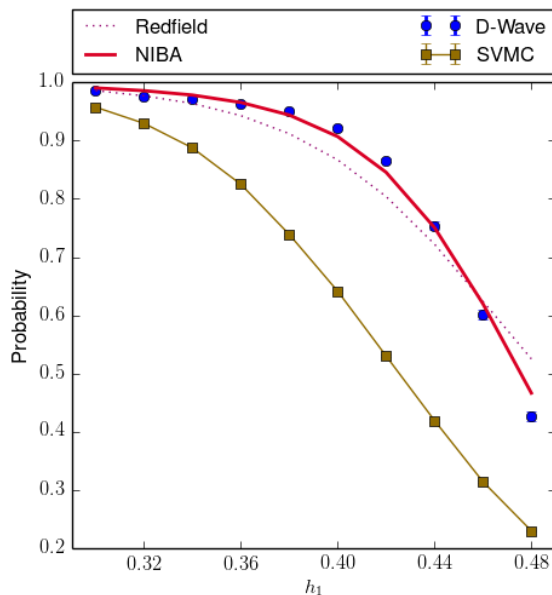


FIG. 14. Probability of success versus  $h_1$  for D-Wave (purple  $\circ$  marker), open system quantum numerics and the classical-path model (SVMC, brown  $\square$  marker). The open system numerics are obtained from the Redfield quantum master equation based on the transition rate (26) (dotted line) and from the NIBA Quantum Master Equation (continuous red line). The NIBA Quantum Master Equation is a surprisingly good fit to the data. Error bars are smaller than markers.

#### D. Numerical simulation of classical paths

Our main purpose is to study multiqubit tunneling under experimental conditions with current technology for programmable quantum annealing, such as the D-Wave Two chip. One important component of this study is the comparison to the detailed open quantum system theory outlined in the previous section. In addition, we will compare the experimental data with semi-classical numerics that simulate the evolution under the effective potential  $U(q_1, q_2, s)$ , as introduced in Sec. II C. We are interested in numerical

methods that fulfill the following conditions:

- They must be constrained to quantum product states, quantum correlations are disallowed.
- They do not include collective state or cluster updates. This prevents quantum tunneling to be included in the simulation. The dynamical equations of the numerical method must specify only equations of motion for each individual qubit in the product state
- The simulation must be capable of including the effective potential  $U(q_1, q_2, s)$  of Sec. II C.

One such method was introduced recently in Ref. [41] and studied in related works [42, 45]. For these methods, dynamics are constrained to spin-vector product states, with one spin vector per qubit. For a given product state, we denote by  $\theta_\mu$  the angle of the spin vector for qubit  $j$  with the  $x$  quantization axis. For a given Hamiltonian  $H_0(s)$ , we denote the corresponding energy by  $E_s(\theta_1, \dots, \theta_{n_q})$ , where  $n_q$  is the number of qubits. The evolution consists of a sequence of sweeps along the Hamiltonian path  $\{H_0(s)\}$ . In each sweep, a Monte Carlo update is proposed for each qubit in the following manner:

- A new angle  $\theta'_\mu$  is drawn from the uniform distribution in  $[0, 2\pi]$ .
- The spin vector for qubit  $j$  is updated  $\theta_\mu \leftarrow \theta'_\mu$  according to the Metropolis rule for the energy difference

$$D = E_s(\dots, \theta'_\mu, \dots) - E_s(\dots, \theta_\mu, \dots).$$

That is, the move is always accepted if  $D$  is negative, and with probability given by the Boltzmann factor  $\exp(-D/k_B T)$  if  $D$  is positive.

We call this method Spin Vector Monte Carlo (SVMC). The initial state is chosen to be the global minimum of the transverse field. When the spin vectors of each cluster are aligned with the parameters  $\{q_1, q_2\}$  we obtain  $E_s(q_1, \dots, q_2) = U(q_1, q_2, s)$ . For low  $T$  and sufficient sweeps, the evolution proceeds along the false minima path of Fig. 5. That is, the numerical method at low temperature simulates the classical-path model outlined in Sec. II C.

This numerical method allows us to study thermal hopping between the minima of the effective potential  $U(q_1, q_2, s)$ . To check this correspondence, we studied the height of the energy barrier obtained from Kramer's theory applied to SVMC. For the potential  $U(q_1, q_2, s)$  at a fixed value of  $s$ , we initialized the spin vector state at a local minima, and watch for Kramer events. A Kramer event corresponds to the arrival at the other minima under thermal activation. According to Kramer's theory, the dependence on temperature for the expected number of sweeps necessary for a Kramer event follows the formula  $\exp(\Delta U/T)$ , where  $\Delta U$  is the height of the energy barrier. We extract the energy barrier by fitting the curve of the average number of sweeps for different  $T$ . We find that this matches almost exactly the energy barrier height

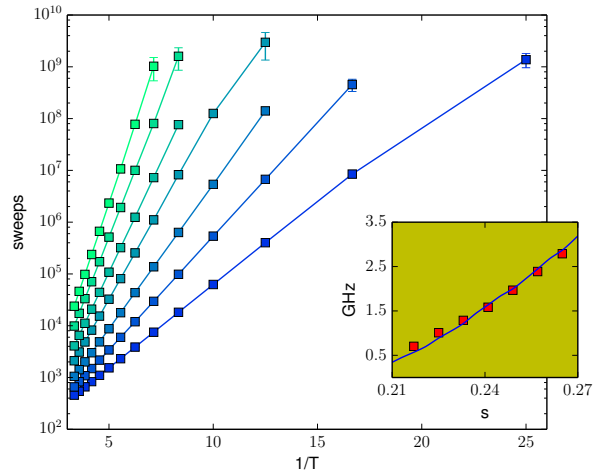


FIG. 15. Analysis of the activation energy for Kramer's escape for SVMC. The main figure shows, in a semilog scale, the average number of sweeps as a function of temperature. We plot lines for different points in the annealing schedule, from  $s = 0.217$  (dark blue) to  $s = 0.265$  (green). The embedded figure shows the activation energy (red dots) and the semi-classical energy barrier (blue). There is a good correspondence between SVMC and the effective energy potential.

from  $U(q_1, q_2, s)$  in Fig. 6 for different values of  $s$ , see Fig. 15. We also studied other semi-classical methods, such as a mean-field Redfield model similar to Forster's theory, and a Landau-Lifshitz-Gilbert model related to the one studied in Ref. [72]. As we could not recover the barrier height of the effective energy potential  $U(q_1, q_2, s)$  from the Kramer events with these other numerical methods, we will use SVMC in what follows.

A disadvantage of SVMC as outlined above and introduced in Ref. [41] is that there is no natural choice to relate the number of sweeps to the physical evolution time. As in other works, we will choose the number of sweeps in order to obtain a good correlation with the probability of success of the D-Wave chip for a benchmark of random Ising models with binary couplings  $J_{\mu\nu} \in \{1, -1\}$  [36, 39, 41, 45]. This will allow us to phenomenologically correlate the number of sweeps to physical time. We set the algorithmic temperature of SVMC to be the same as the physical temperature because we are interested in the dependence of the success probability with temperature. There are no important differences for the correlation with other temperature choices. The correlation with the random Ising benchmark for 128,000 sweeps (see Fig. 16) is 0.92, and the residual probabilities  $p_{\text{SVMC}} - p_{\text{D-Wave}}$  have a mean of 0.05 and a standard deviation of 0.12. This is consistent with the best values found over a wide range of parameters. We will use 128,000 sweeps at 15 mK as our reference rate for the rest of the paper.

Another parameter, the so-called qubit background susceptibility  $\chi$ , has been introduced in the literature to improve the correlations between numerical simulations and the D-Wave data [42, 45]. While the phys-

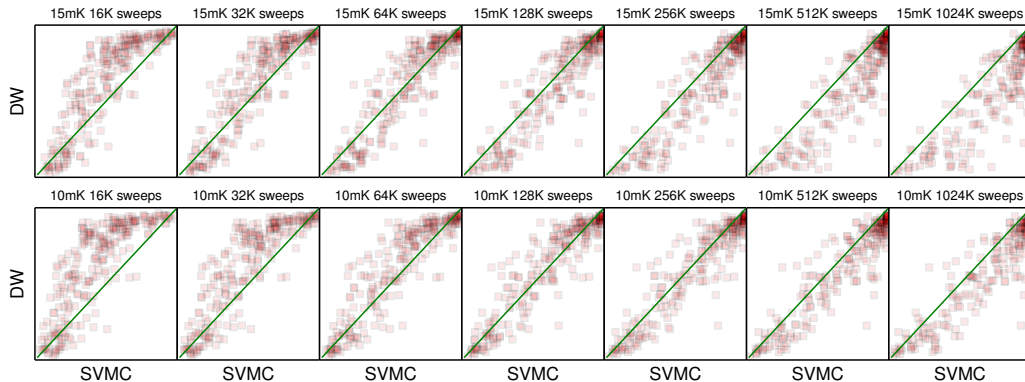


FIG. 16. Scatter plots showing the correlation of D-Wave Two data and SVMC for the random Ising benchmark for different algorithmic temperatures (in mK) and number of sweeps. We will use the parameters  $T = 15$  mK, and sweeps = 128,000 in the rest of the paper.

ical motivation for this parameter is well understood, it is also treated in those works as a free parameter together with the number of sweeps. Increasing values of  $\chi$  have the effect of decreasing the barrier height for  $h_1 < J/2$ . We have designed a specific problem to bound the range of choices of  $\chi$  for SVMC compatible with experimental data. We find  $\chi = 0.0025$  to be the value most consistent with the data for the device used in our paper, as seen in App. D. Plots that include this choice of  $\chi$  for SVMC are also presented in the Appendix.

#### IV. EXPERIMENTAL RESULTS FROM THE D-WAVE TWO PROCESSOR AND FIT TO THEORY

##### A. Double-well potential with two clusters

One of the most distinctive signatures of quantum tunneling when compared to thermal hopping is the response to temperature variations at low temperatures. Consider first the quantum tunneling situation. For low temperatures compared to the gap, and when the tunneling rate is fast compared to the evolution time, the final success probability is close to unity. As we increase the temperature in the range of the gap, we expect to see thermal excitations and a lower probability of success. Therefore, the expected tendency at low temperatures is a decrease of probability of success with increasing temperature.

Consider now the situation with thermal hopping. At very low temperatures, the state follows the classical path along the local minimum through the evolution. If this path does not connect to the global minimum, the probability of success is close to zero. As we increase the temperature, we also increase the probability of a thermal excitation over the energy barrier, and therefore increase the probability of success. Consequently, the expected tendency at low temperatures is an increase in the probability of success for models that follow the classical paths.

Figure 17 shows the success probability as a function of temperature for D-Wave, open system quan-

tum numerics and the classical-path model (SVMC) for  $h_1 = 0.44$  in the Hamiltonian of Eq. (4). There is a clear tendency towards lower probability of success as temperature increases in the experimental D-Wave data. The same is true of the various open system quantum master equations models. This is a consequence of quantum tunneling. Interestingly, SVMC shows a positive correlation between success probability and temperature. This is a consequence of thermal hopping above the energy barrier. The probability of success obtained with the Redfield quantum master equation matches well the D-Wave data, and it is not affected by the control noise of the D-Wave chip. SVMC is run at an algorithmic temperature equal to the physical temperature indicated in the horizontal axis, and with 128,000 sweeps, as explained in Sec. IIID. We plot SVMC without control noise and SVMC with the physically estimated control noise. Averaging over control noise does not have a significant effect on the probability of success for SVMC. As seen in Figure 14, the NIBA Quantum Master Equation model is a better match to the data than the Redfield model. In the region  $h_1 < 0.5$  there is an energy barrier between the local and global minimum. In this region, we see that the probability of success for SVMC is significantly lower than the probability of success for D-Wave and open system quantum models.

Figure 18 shows the probability of success versus temperature for D-Wave data and SVMC numerics for  $h_1 = [0.38, 0.4, 0.42, 0.44, 0.46, 0.48]$ . The probability of success decreases with temperature for D-Wave in instances with a significant coherent tunneling contribution to the dynamics. For SVMC the probability of success increases with temperature in all cases. As noted before, the probability of success from SVMC is lower than the probability of success of D-Wave. Figure 19 shows the probability of success versus temperature for D-Wave data and open quantum systems numerics for the same values of  $h_1$ . The D-Wave data reproduces the reduction in probability of success predicted by the quantum models. The probability of success does increase with temperature for D-Wave for the instance with  $h_1 = 0.48$ , where the minimum gap is 10 MHz. The limitation in this case is strong

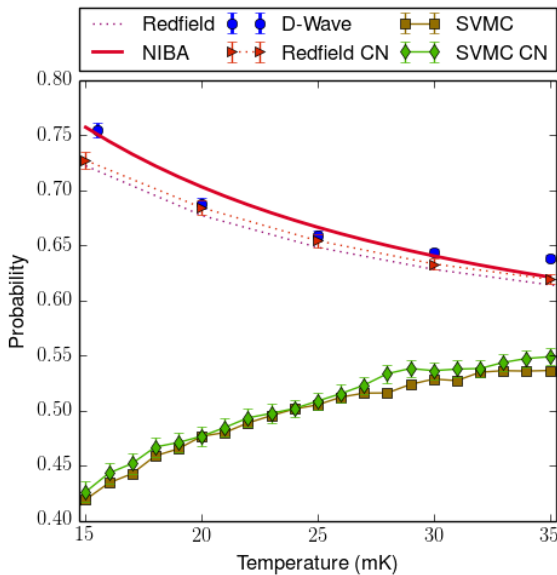


FIG. 17. Probability of success versus temperature at  $h_1 = 0.44$  for D-Wave (purple  $\circ$  marker), open system quantum numerics and the classical-path model (SVMC). The open system numerics are Redfield (dotted line), Redfield with physically estimated control noise of  $\sigma_h = 0.05$  for the local fields and  $\sigma_J = 0.035$  for the couplings (dotted line with  $\triangleright$  marker) and the NIBA Quantum Master Equation (continuous red line). The two SVMC curves correspond to SVMC (brown  $\square$  marker) and SVMC with the physically estimated control noise of  $\sigma_h = 0.05$  for the local fields and  $\sigma_J = 0.035$  for the couplings (SVMC-CN, green  $\diamond$  marker). Error bars are smaller than markers when not seen. D-Wave data fits well the quantum models. The temperature dependence of SVMC is the opposite. It is important to emphasize that in this temperature range the lowest two energy states (the ones that participate in the double well potential) account for all the probability (0.9998 in the experimental D-Wave data, 0.99998 for SVMC).

coupling to low frequency noise. This behavior is not captured by standard Redfield theory. To explain it, we must take into account the reorganization energy induced by low frequency noise, as in standard Marcus theory. The NIBA Quantum Master Equation does capture this effect correctly. For this gap size, coherent quantum tunneling is suppressed.

### B. Larger problems that contain the weak-strong cluster “motives” as subproblems

In the previous sections we established that quantum tunneling assists the D-Wave Two processor in finding the global minimum of the weak-strong cluster probe problem. The 16 qubit problem we considered was specifically designed to be suitable for studying the role of tunneling by analytical, numerical and experimental means. A generalization to a larger number of qubits is achieved by studying problems that contain the weak-strong cluster “motive” multiple times within the connectivity graph.

The first generalized configuration we studied is a

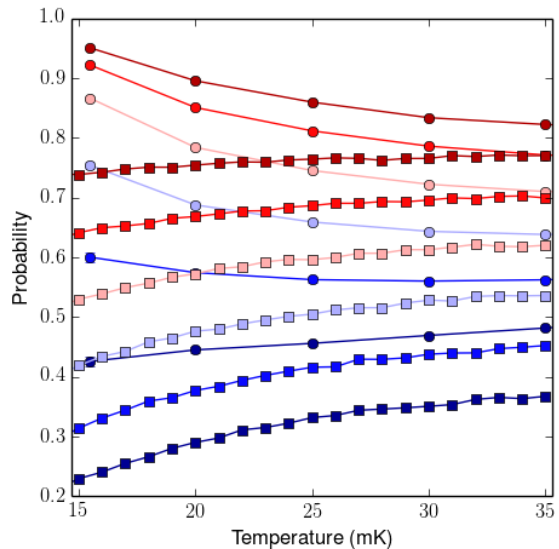


FIG. 18. Probability of success versus temperature for D-Wave data ( $\circ$  markers) and SVMC numerics ( $\square$  markers). We plot (from top to bottom, and red to blue)  $h_1 = [0.38, 0.4, 0.42, 0.44, 0.46, 0.48]$ . Error bars are smaller than markers. We use SVMC with 15 mK algorithmic temperature and 128,000 sweeps, as explained in the text.

stack of weak-strong cluster pairs with  $h_1 = 0.4$  setting all connections between the left columns of the unit cells in the Chimera graph to ferromagnetic 1 (see Fig. 21a). As the number of stacked cluster pairs grows, the success probability decreases for the annealing time of 20  $\mu$ s that was used in the previous sections. This behavior is expected since the minimum gap also decreases. When we increase the annealing time to 20 ms the success probability grows significantly. The increase of the success probability for SVMC is much slower with a proportional increase in the number of sweeps (note the logarithmic scale) even for instances with 128 qubits, see Fig. 22.

In a second experiment we again placed a number of weak-slow cluster pairs across the Chimera graph. Then we connected the strong clusters in a glass like structure by randomly setting all Chimera connections between neighboring pairs of strong clusters to +1 or -1. Fig. 21b depicts a problem instance constructed this way. The success probabilities are shown in Fig. 23. We fit the average probability  $p(n_q)$  as  $p(n_q) \propto \exp(-\alpha n_q)$ , where  $n_q$  is the number of qubits. The fitting exponent  $\alpha$  for the D-Wave data is  $-(1.1 \pm 0.05) \cdot 10^{-2}$ , while the fitting exponent for the SVMC numerics is  $-(2.8 \pm 0.17) \cdot 10^{-2}$ . For additional data including problems for which the strong fields have been set to zero please refer to Appendix C.

## V. CONCLUSION

There has been a great deal of debate as to whether quantum resources in the D-Wave Two processor are employed in a manner that enhances the probability



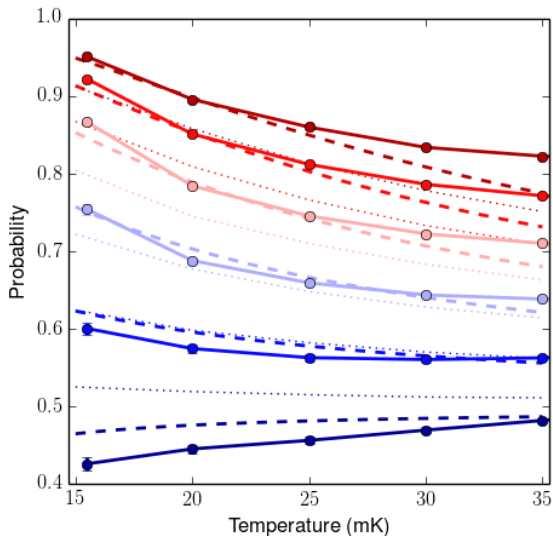


FIG. 19. Probability of success as a function of temperature for  $h_1 = [0.38, 0.4, 0.42, 0.44, 0.46, 0.48]$ . We plot D-Wave data ( $\circ$  markers), Redfield (dotted line) and the NIBA Quantum Master Equation (dashed line). The main qualitative difference is that for  $h_1 = 0.48$  the NIBA Quantum Master Equation predicts a much lower probability of success, which increases with temperature. We see the same feature in D-Wave’s experimental data. In the NIBA Quantum Master Equation, this is due to the suppression of the tunneling rate by the low-frequency noise. The gap at the avoided crossing for  $h_1 = 0.48$  is 10 MHz. The standard Redfield model does not include low-frequency noise.

for the device to return low energy solutions of encoded optimization problems. To address this question we programmed optimization problems corresponding to two weakly coupled ferromagnetic clusters with strong intra-cluster interactions and local fields acting on two clusters in the opposite directions. This construction encodes the simplest non-convex optimization problem that only exhibits one false and one global minimum in a time-dependent effective potential. The time evolution is such that a path in the potential over product states connects the initial global minimum with the final false minimum. The final global minimum can only be reached by traversing an energy barrier. Experimentally, we found that for this situation the D-Wave Two quantum annealer returns the solution that minimizes the energy with consistently higher probability than physically plausible models of the hardware that only employ product states which do not allow for multiqubit tunneling transitions. On the contrary open system quantum mechanical models are in a very close correspondence with the hardware data without using any fitting parameters. We developed a multiqubit Quantum Master Equation using the Non Interacting Blip approximation (NIBA) which takes high and low frequency noise into account. It continuously rotates the basis in multiqubit Hilbert space to coincide with the basis that minimizes the transition rate be-

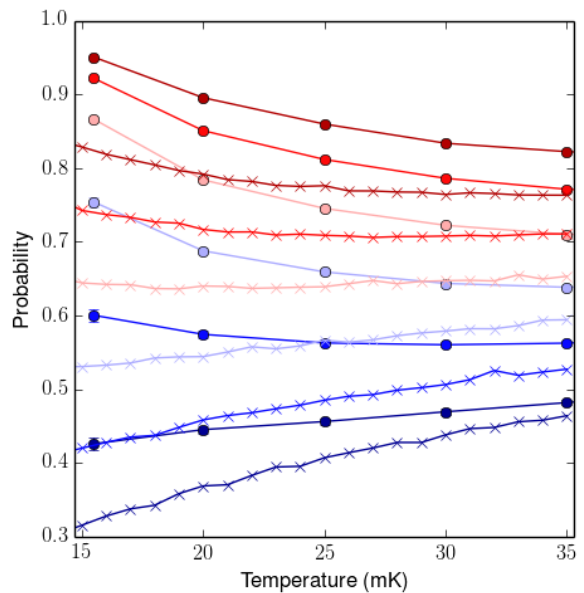


FIG. 20. Probability of success versus temperature for D-Wave data ( $\circ$  markers) and Quantum Annealing Path Integral Monte Carlo Quantum Annealing (PIMC-QA) numerics ( $\times$  markers). We plot (from top to bottom, and red to blue)  $h_1 = [0.38, 0.4, 0.42, 0.44, 0.46, 0.48]$ . Error bars are smaller than markers. PIMC-QA is not a good fit to D-Wave’s data.

tween the first two levels. In this way we find the most robust states under decoherence. One can think of this as working in the instantaneous pointer basis [66, 73]. The polaron transform was used since the interaction of the qubits with their oscillator baths forms polaron-like quasi particles. To increase our confidence that quantum mechanical models are indeed required to describe the D-Wave annealing dynamics properly, we performed a series of experiments in which we varied the temperature of the chip. Regardless of specific parametrizations of quantum and classical models, the apparent trend between temperature and success probability revealed by these experiments is consistent only with quantum models.

Quantum correlations are strongest during the annealing near the avoided crossing. In our problem fast collective tunneling processes involving many qubits near the avoided crossing give rise to adiabatic eigenstates where the states of the 8 spins forming a tunneling cluster contain quantum correlations. Environmental effects modify the ideal system (adiabatic) states into pointer states that still retain quantum superpositions (non-product nature). In this our study is different from the previous study of incoherent qubit tunneling near the minimum point observed using the D-Wave-I chip [33].

In contrast to a simple 2-level system tunneling, the overlap between the states is relatively large at the point of minimum gap, and decreases exponentially after that. The initial overlap gives rise to fast transitions and thermalization which is maintained throughout the avoided crossing region. After the avoided crossing the energy splitting increases, leading to ther-



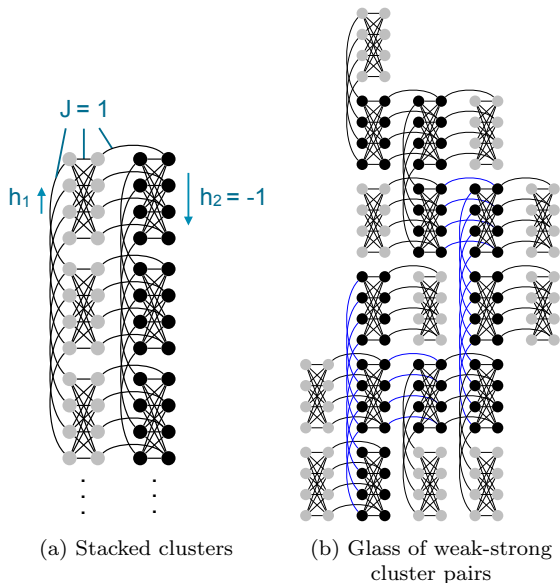


FIG. 21. Larger problems that contain the weak-strong cluster “motives” as subproblems. (a) A stack of weak-strong cluster pairs. (b) Weak-strong cluster pairs connected in a glassy fashion by setting all connections between any two neighboring strong clusters randomly to either  $-1$  or  $+1$ . The  $-1$  anti-ferromagnetic connections are depicted in blue.

mal de-population of the excited state. Transitions slow down because of the steep decrease of the collective tunneling matrix elements. Eventually, the population of the excited state freezes at the point where the transition rate is reduced to the level of the quantum annealing rate. It should be noted that the freezing described here is a multiqubit effect that is to be distinguished from the single qubit freezing that occurs at the end of the annealing evolution due to the raising of the barrier of the individual qubits. Higher temperature will lead to greater thermal population of the excited state at this freezing point, and to the decrease of the success probability. This results in the opposite temperature effect compared to the limit of incoherent tunneling, where the level population immediately after avoided crossing is inverted (the excited state has a larger population). In this case an increase of temperature would lead to an increase of the success probability.

In our studies we employed single qubit noise model parameters reconstructed from the MRT studies of D-Wave One [31] and D-Wave Two systems. Results for the 16 qubit quantum annealing success rates are in remarkably close correspondence with experimental data over the range of local fields and temperatures studied here (see Fig. 14).

The correlation between D-Wave’s experimental data and Path Integral Monte Carlo along the Quantum Annealing schedule (PIMC-QA) has been studied in recent works [36, 39, 45]. Unfortunately, there is no known formal connection between Monte Carlo updates in PIMC-QA and open system quantum dynamics. The relationship between PIMC-QA and quantum tunneling is also not well understood. We show

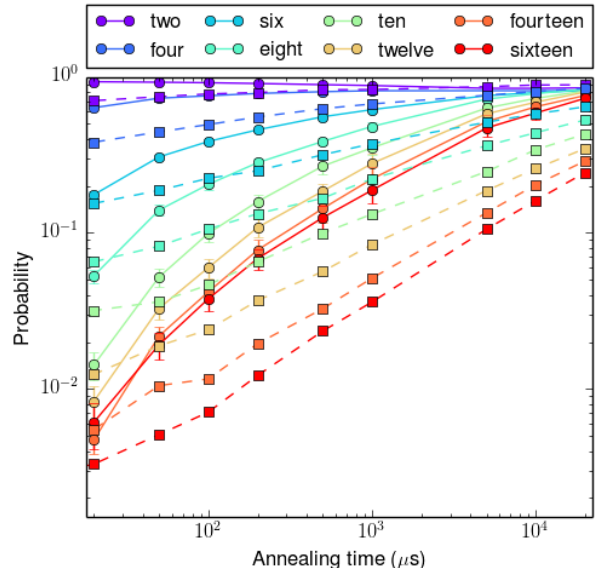


FIG. 22. Success probabilities for varying numbers of stacked weak-strong cluster pairs as a function of annealing time for a weak local field  $h_1 = 0.4$  and  $J = 1$ . The different colors show ‘two’ clusters, one ‘weak’ and one ‘strong’, as in Sec. IV A, ‘four’ clusters (two weak, two strong), ‘six’ clusters (as in Fig. 21a), etc... We show D-Wave data ( $\circ$  marker, continuous lines) and SVMC ( $\square$  marker, dashed lines). Note that for larger number of qubits the success probability for the D-Wave increases faster with annealing time than for SVMC with a proportional increase in the number of sweeps.

in Fig. 20 the probabilities for PIMC-QA as a function of temperature for different values of  $h_1$ . We use similar parameters for PIMC-QA as in Ref. [36]. The probability of success for PIMC-QA is lower than the probabilities observed for D-Wave. On the one hand, there is an inverse relationship between temperature and success probability for small  $h_1/J$  ratios (big minimum gaps in the QA spectrum). On the other hand, this dependence is opposite to D-Wave’s data for  $h_1 = 0.44$ , the main case studied in Sec. IV A.

Beyond the original 16 qubit probe problem we also explore larger problems of up to 200 qubits that contain multiple weak-strong cluster pairs. We found that classical-path models that only operate on product states do not explain the hardware performance. The difference in the fitting exponents is given in Sec. IV B. Appendix C contains the fitting exponents for different choices of parameters of SVMC and PIMC-QA.

A way to think of multiqubit tunneling as a computational resource is to regard it as a form of large neighborhood search. Collective tunneling transitions involving  $K$  qubits explore a  $K$  variable neighborhood. We find that the current generation D-Wave Two annealer enables tunneling transitions involving at least 8 qubits. It will be an important future task to determine the maximal  $K$  for the current hardware and how large it can be made in next generation hardware. The larger  $K$ , the easier it should be to translate the quantum resource “ $K$ -qubit tunneling” into a computational speedup. We want to emphasize that we do

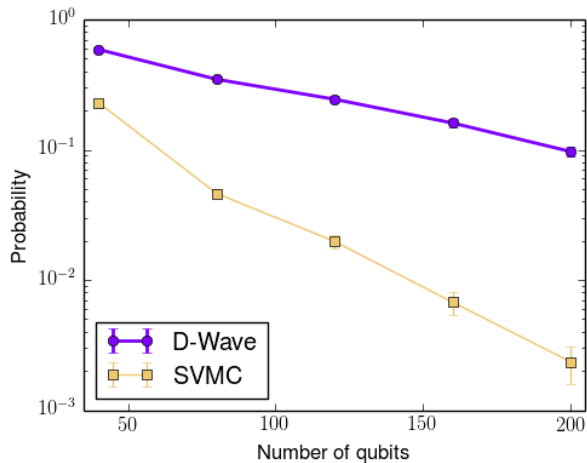


FIG. 23. Success for a glass of weak-strong clusters as a function of the number of qubits involved. D-Wave data is plotted with purple  $\circ$  markers. SVMC is plotted with  $\square$  markers. The fitting exponent for the D-Wave data is  $-(1.1 \pm 0.05) \cdot 10^{-2}$ , while the fitting exponent for the SVMC numerics is  $-(2.8 \pm 0.17) \cdot 10^{-2}$ . The error estimates for the exponents are obtained by bootstrapping.

not claim to have established a quantum speedup in this work. To this end one would have to demonstrate that no known classical algorithm finds the optimal solution as fast as the quantum process. To establish such an advantage it will be important to study to what degree collective tunneling can be emulated in classical algorithms by employing cluster update methods. However the collective tunneling phenomena demonstrated here present an important step towards what we would like to call a *physical speedup*: a speedup relative to a hypothetical version of the hardware operated under the laws of classical physics.

To summarize, in this work, we demonstrate that a noticeable computational role of collective tunneling can already be observed in existing quantum annealing hardware, such as the D-Wave Two processor. This is despite substantial environmental noise and control errors. Our study can thus inspire the design and development of future generations of powerful medium- or large-scale quantum information processors that utilize collective tunneling as a useful quantum-computational resource. Future designs might operate under longer coherence times, reduced control errors, higher graph connectivity, and benefit from advanced quantum error protection or correction procedures. Such improvements might be necessary to convert the collective tunneling resource into a computational advantage.

**Acknowledgements** – We would like to thank Edward Farhi and John Martinis for reviewing and discussing earlier versions of the paper. We also thank Ryan Babbush and Bryan O’Gorman for reviewing the manuscript, and Damian Steiger, Daniel Lidar and Tameem Albash for comments about the tem-

perature experiment. The work of V.N.S. was supported in part by the Office of the Director of National Intelligence (ODNI), Intelligence Advanced Research Projects Activity (IARPA), via IAA 145483 and by the AFRL Information Directorate under grant F4HBKC4162G001.

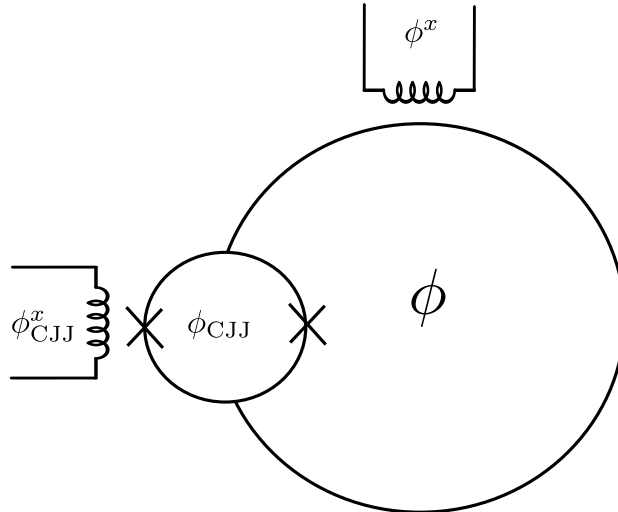


FIG. 24. Schematic of a Compound Josephson Junction (CJJ) qubit.

## Appendix A: Single Flux Qubit Hamiltonian

### 1. Full Flux Qubit Hamiltonian

The full Compound Josephson Junction (CJJ) flux qubit Hamiltonian is better expressed in terms of flux phases, defined as renormalized fluxes  $\phi = 2\pi\Phi/\Phi_0$  for any flux  $\Phi$ . The Hamiltonian is [24]

$$-E_C\partial_\phi^2 - E_{C_{CJJ}}\partial_{\phi_{CJJ}}^2 + E_J \cos(\phi) \cos(\phi_{CJJ}/2) + E_L \frac{(\phi - \phi^x)^2}{2} + E_{L_{CJJ}} \frac{(\phi_{CJJ} - \phi_{CJJ}^x)^2}{2}, \quad (\text{A1})$$

where  $\phi$  is the body flux phase to be quantized,  $\phi^x$  is the external flux phase,  $\phi_{CJJ}$  is the flux phase of the CJJ and  $\phi_{CJJ}^x$  is the external flux of the CJJ (see Fig. 24). The energies of the different terms are given by

$$\begin{aligned} E_C &= \frac{(2e)^2}{2C} & E_{C_{CJJ}} &= \frac{(2e)^2}{2(C/2)} & E_J &= \frac{I_c\Phi_0}{2\pi} \\ E_L &= \left(\frac{\Phi_0}{2\pi}\right)^2 \frac{1}{L + L_{CJJ}/4} & E_{L_{CJJ}} &= \left(\frac{\Phi_0}{2\pi}\right)^2 \frac{1}{L_{CJJ}} \end{aligned}$$

The parameters are the capacitance  $C$ , the body inductance of the main flux loop  $L$  and of the Compound Josephson Junction  $L_{CJJ}$ , and the effective critical current of the Compound Josephson Junction  $I_c$ .

The median values for D-Wave's CJJ flux qubits in GHz are

$$\begin{aligned} \frac{E_C}{2\pi\hbar} &= 0.67 \text{ GHz} & \frac{E_{C_{CJJ}}}{2\pi\hbar} &= 1.35 \text{ GHz} & \frac{E_J}{2\pi\hbar} &= 1071 \text{ GHz} \\ \frac{E_L}{2\pi\hbar} &= 537 \text{ GHz} & \frac{E_{L_{CJJ}}}{2\pi\hbar} &= 11680 \text{ GHz} & & \end{aligned}$$

The CJJ flux phase  $\phi_{CJJ}^x$  controls the quantum annealing evolution. The function  $\phi_{CJJ}^x(s)$  as a function of the annealing parameter for the quantum annealing schedule employed in this paper is plotted in Fig. 25.

Because  $E_{L_{CJJ}} \gg E_L$  the phase  $\phi_{CJJ}$  can be assumed to be centered at the value given by  $\phi_{CJJ}^x$ , as a first approximation. The approximated flux qubit Hamiltonian is then

$$\mathcal{H}_s(\phi^x) = -E_C\partial_\phi^2 + E_J \cos(\phi) \cos(\phi_{CJJ}^x(s)/2) + E_L \frac{(\phi - \phi^x)^2}{2}. \quad (\text{A2})$$

This potential is plotted in Fig. 26a.

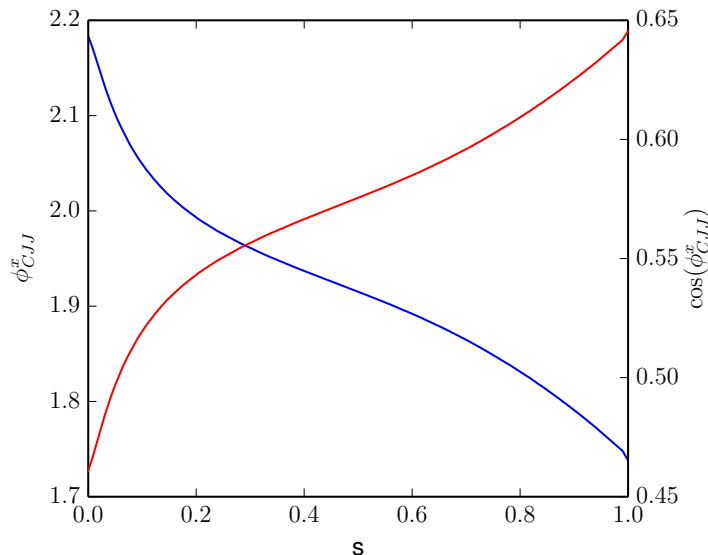
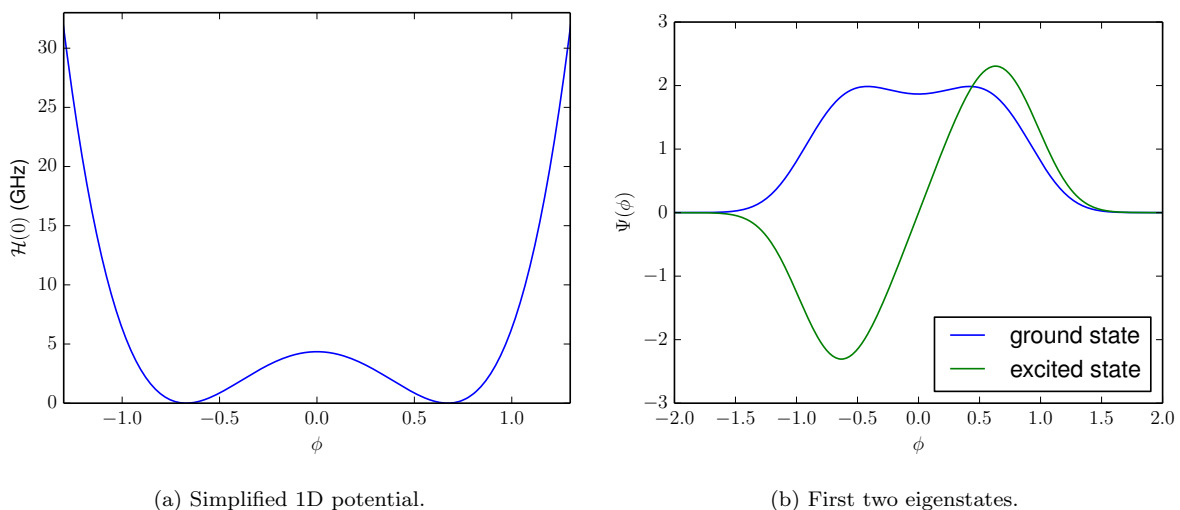


FIG. 25. The CJJ external phase  $\phi_{CJJ}^x$  (blue) and  $\cos(\phi_{CJJ}^x)$  (red). The dependence of  $\phi_{CJJ}^x$  on the parameter  $s$  is chosen so that the persistent current  $I_p(s)$  scales linearly with  $s$ , see Eq. (A16).



(a) Simplified 1D potential.

(b) First two eigenstates.

FIG. 26. (a) The simplified 1D potential  $\mathcal{H}(\phi^x)$  of Eq. (A2) for annealing parameter  $s = 0.278$ . (b) The first two eigenvectors of the flux qubit potential for  $s = 0.278$ .

## 2. Effective qubit Hamiltonian

The effective qubit Hamiltonian is the simplified Hamiltonian  $\mathcal{H}_s(\phi^x)$  of Eq. (A2) projected into the two lowest energy levels  $\{|\mathbf{g}(s)\rangle, |\mathbf{e}(s)\rangle\}$  of  $\mathcal{H}_s(0)$

$$\mathcal{H}_s(\phi_x) \Big|_{\{|\mathbf{g}(s)\rangle, |\mathbf{e}(s)\rangle\}} = \mathcal{H}_s(0) + \phi^x \frac{\partial \mathcal{H}_s(0)}{\partial \phi^x} \Big|_{\{|\mathbf{g}(s)\rangle, |\mathbf{e}(s)\rangle\}}. \quad (\text{A3})$$

The eigenvectors of  $\mathcal{H}_s(0)$  are symmetric and anti-symmetric superpositions of the flux up and down state in the double-well potential (see Fig. 26b)

$$|\mathbf{g}(s)\rangle = \frac{1}{2}(|\uparrow(s)\rangle + |\downarrow(s)\rangle) \quad (\text{A4})$$

$$|\mathbf{e}(s)\rangle = \frac{1}{2}(|\uparrow(s)\rangle - |\downarrow(s)\rangle). \quad (\text{A5})$$

The gap between the ground state and the third excited state, depending on the annealing parameter  $s$ , goes between 10 and 8 GHz in the region of interest. This justifies the projection into the two lowest energy levels as long as the linear term in  $\phi_x$  remains well below this energy.

Note that

$$\phi^x \frac{\partial \mathcal{H}_s(0)}{\partial \phi^x} = \Phi^x \frac{\Phi}{L + L_{\text{CJJ}}/4}, \quad (\text{A6})$$

where  $\Phi^x$  is the external flux and  $\Phi/(L + L_{\text{CJJ}}/4)$  is the persistent current operator. The eigenvectors of this operator are the flux up and down states  $|\uparrow(s)\rangle, |\downarrow(s)\rangle$ , with eigenvalues  $\pm I_p(s)$ . This defines the persistent current  $I_p(s)$ . We denote the gap between these states by  $\Delta_1(s)$ . In the basis of the up and down flux states we write

$$\mathcal{H}_s(0) + \phi^x \frac{\partial \mathcal{H}_s(0)}{\partial \phi^x} \Big|_{\{|\mathfrak{g}(s)\rangle, |\mathfrak{e}(s)\rangle\}} = -\frac{1}{2}(\Delta_1(s)\sigma^x + \epsilon_1(\phi^x)\sigma^z), \quad (\text{A7})$$

where

$$\epsilon_1(\phi^x) = 2I_p(s)\Phi^x \quad (\text{A8})$$

$$\Phi/(L + L_{\text{CJJ}}/4) = I_p(s)\sigma^z, \quad (\text{A9})$$

in this basis.

### 3. Coupling between qubits

The coupling between qubits has the form [74]

$$-J_{\mu\nu}E_M(\phi_\mu - \phi_\mu^x)(\phi_\nu - \phi_\nu^x) \approx -J_{\mu\nu}E_M\phi_\mu\phi_\nu, \quad (\text{A10})$$

where  $J_{\mu\nu} \in [-1, 1]$  is the dimensionless coupling. The corresponding energy is

$$\frac{E_M}{2\pi\hbar} = \frac{1}{2\pi\hbar} \left( \frac{\Phi_0}{2\pi} \right)^2 \frac{M_{\text{AFM}}}{(L + L_{\text{CJJ}}/4)^2} = 2.44 \text{ GHz}, \quad (\text{A11})$$

where in our case  $M_{\text{AFM}}$  is measured to be 1.41 pico henries.

In the two level qubit Hamiltonian approximation we use  $\Phi/(L + L_{\text{CJJ}}/4) \equiv I_p(s)\sigma^z$  to write

$$-J_{\mu\nu}E_M\phi_\mu\phi_\nu \approx -J_{\mu\nu}M_{\text{AFM}}I_p^2(s)\sigma_\mu^z\sigma_\nu^z = -B(s)J_{\mu\nu}\sigma_\mu^z\sigma_\nu^z, \quad (\text{A12})$$

with the annealing function  $B(s)$  defined as  $B(s) = M_{\text{AFM}}I_p^2(s)$ . The superconducting flux qubits are calibrated so that  $I_p(s)$  is the same for each of them.

### 4. External flux phase $\phi^x$

The value of the external flux phase  $\phi^x$  controls the strength of the local field in the single qubit Hamiltonian of Eq. (A7). Note that  $B(s)$ , as defined above, scales with the persistent current squared. This is the reason why the external field flux is chosen (using our sign convention) as  $\Phi^x = hM_{\text{AFM}}I_p(s)$  so then (see Eq. (A8))

$$\epsilon_1(\phi^x) = 2hM_{\text{AFM}}I_p^2(s) = 2hB(s). \quad (\text{A13})$$

Here  $h \in [-1, 1]$  is the dimensionless value of the local field as in Eq. (1) With this choice we write the annealing Hamiltonian as in Eq. (1):

$$H_0(s) = -\frac{1}{2}\Delta_1(s) \sum_{\mu} \sigma_{\mu}^x - \frac{1}{2}\epsilon_1(\phi^x)\sigma_{\mu}^z - \sum_{\mu\nu} J_{\mu\nu}E_M\phi_{\mu}\phi_{\nu} \quad (\text{A14})$$

$$= -A(s) \sum_{\mu} \sigma_{\mu}^x - B(s) \left( \sum_{\mu} h_{\mu}\sigma_{\mu}^z + \sum_{\mu\nu} J_{\mu\nu}\sigma_{\mu}^z\sigma_{\nu}^z \right). \quad (\text{A15})$$

As mentioned above, the CJJ flux phase  $\phi_{\text{CJJ}}^x$  controls the quantum annealing evolution. Its value  $\phi_{\text{CJJ}}^x(s)$  plotted in Fig. 25 was chosen so that  $I_p(s)$  scales linearly. In our case we have, for the Google-NASA D-Wave Two chip,

$$M_{\text{AFM}}I_p(s) \frac{2\pi}{\Phi_0} \approx 10^{-3}(4.11s + 1.21). \quad (\text{A16})$$

The energy functions  $A(s)$  and  $B(s)$  are shown in Fig. 1.



## 5. Coupling to the bath

The interaction Hamiltonian of a single qubit with the bath is dominated by fluctuations on the flux body bias. The dimensional interaction Hamiltonian is

$$\mathcal{H}_{\text{SB}} = \hat{I}\delta\Phi_x = \frac{\hat{\Phi} - \Phi_x}{L}\delta\Phi_x. \quad (\text{A17})$$

Projecting into the subspace  $\{|g(s)\rangle, |e(s)\rangle\}$  as before we write (see Eq. (A9))

$$\mathcal{H}_{\text{SB}}(s) = I_p(s)\sigma^z\delta\Phi_x = \frac{1}{2}\sigma^z Q(s) \quad (\text{A18})$$

where

$$Q(s) = 2I_p(s)\delta\Phi_x. \quad (\text{A19})$$

The flux bias fluctuations are measured using microscopic resonant tunneling (MRT), as mentioned in the text. In particular MRT is performed at a point  $s$  with small tunneling amplitude  $\Delta < 1$  MHz. Under these conditions we obtain the parameters for the noise spectral density  $S_{\text{MRT}}(\omega)$  which is defined in terms of a correlation function of the bath operators  $Q(s)$  through the equation

$$S(\omega)_{\mu\nu} = \int_0^\infty dt e^{i\omega t} \langle e^{iH_B t} Q_\mu e^{-iH_B t} Q_\nu \rangle, \quad (\text{A20})$$

where  $\mu$  and  $\nu$  are qubit's indexes. From Eq. (A19)

$$\delta\Phi_x = \frac{Q_{\text{MRT}}}{2I_p(\text{MRT})}, \quad (\text{A21})$$

which implies

$$Q(s) = \frac{I_p(s)}{I_p(\text{MRT})} Q_{\text{MRT}} \approx \frac{I_p(s)}{I_p(1)} Q_{\text{MRT}}. \quad (\text{A22})$$

This is the source of the dependence of the noise parameters on the annealing parameter, as mentioned in the text. Note that  $S(\omega)$  in Eq. (A19) is quadratic in  $Q(s)$ . The open system parameters  $W(s)$  and  $\eta(s)$  enter the theoretical model through the function

$$f(\tau, s) = i\epsilon_p(s)\tau + \frac{1}{2}W^2(s)\tau^2 - \frac{\eta}{2\pi} \ln G(\tau). \quad (\text{A23})$$

as given in Eq. (62). The relation to  $S(\omega)$  is given by Eq. (60)

$$f(\tau, s) = \int_{-\infty}^\infty \frac{d\omega}{2\pi} S(\omega, s) \frac{1 - e^{-i\omega\tau}}{(\hbar\omega)^2}. \quad (\text{A24})$$

Consequently, we obtain Eq. (23)

$$\frac{\eta(s)}{\eta_{\text{MRT}}} = \left( \frac{W(s)}{W_{\text{MRT}}} \right)^2 = \frac{B(s)}{B(1)}, \quad (\text{A25})$$

where the last equality follows from  $B(s) \propto I_p^2(s)$ , and the fact that the MRT measurements are done at a point with very small  $\Delta_1$ , very close to  $s = 1$ . The values corresponding to measurements done at the D-Wave Two chip are

$$W_{\text{MRT}}/(2\pi\hbar) = 0.4 \text{ GHz}, \quad \eta_{\text{MRT}} = 0.24. \quad (\text{A26})$$

## Appendix B: Villain representation

In the spin basis  $|M, S\rangle$  for total spin  $S$ , we introduce scaled spin operators  $s^\alpha = S^\alpha/S$  for  $\alpha = x, y, z$ , and  $q = M/S$  an scaled quantum number. Denote  $\epsilon = 1/S$  and

$$s^z|q\rangle = q|q\rangle \quad (\text{B1})$$

$$s^\pm|q\rangle = \sqrt{q + \epsilon - q(q \pm \epsilon)}|q \pm \epsilon\rangle. \quad (\text{B2})$$

We further introduce the canonically conjugated momentum operator  $p = -i\epsilon \frac{\partial}{\partial q}$ . The Villain representation in the limit of small  $\epsilon$  (big  $n$ ) is [47, 75]

$$s^+ = e^{-ip} \sqrt{1 + \epsilon - q(q + \epsilon)} \quad (\text{B3})$$

$$s^- = \sqrt{1 + \epsilon - q(q + \epsilon)} e^{ip}. \quad (\text{B4})$$

These operators are Hermitian conjugates in this representation, and we will see that they have the correct action in the coordinate representations of the wave form

$$|\Psi\rangle = \int dq \Psi(q)|q\rangle. \quad (\text{B5})$$

We will use the property

$$e^{-\epsilon \frac{\partial}{\partial q}} F(q) = \sum_{a=0}^{\infty} \frac{(-\epsilon)^a}{a!} \frac{\partial^a}{\partial q^a} F(q) = F(q - \epsilon). \quad (\text{B6})$$

We get

$$s^+ |\Psi\rangle = \int dq e^{-\epsilon \frac{\partial}{\partial q}} \sqrt{1 + \epsilon - q(q + \epsilon)} \Psi(q)|q\rangle = \int dq \sqrt{1 + \epsilon - (q - \epsilon)q} \Psi(q - \epsilon)|q\rangle \quad (\text{B7})$$

$$= \int dq \sqrt{1 + \epsilon - q(q + \epsilon)} \Psi(q)|q + \epsilon\rangle, \quad (\text{B8})$$

and also

$$s^- |\Psi\rangle = \int dq \sqrt{1 + \epsilon - q(q + \epsilon)} e^{\epsilon \frac{\partial}{\partial q}} \Psi(q)|q\rangle = \int dq \sqrt{1 + \epsilon - q(q + \epsilon)} \Psi(q + \epsilon)|q\rangle \quad (\text{B9})$$

$$= \int dq \sqrt{1 + \epsilon - q(q - \epsilon)} \Psi(q)|q - \epsilon\rangle \quad (\text{B10})$$

Ignoring factors of order  $\epsilon$  in Eqs. (B3) and (B4) we approximate

$$s^x = \frac{1}{2}(s^+ + s^-) \approx \sqrt{1 - q^2} \cos p. \quad (\text{B11})$$

We can check the adequacy of the semiclassical Hamiltonian above even for  $n = 8$  from the qualitative agreement of the gap of the original Hamiltonian and that obtained from the semiclassical Hamiltonian by the standard instanton method [6, 47, 75]. From the definition of the momentum operator  $p = -i\epsilon \frac{\partial}{\partial q}$  we see that  $\epsilon = 1/S$  plays the role of  $\hbar$  in the WKB approximation, and we write the WKB ansatz for the semiclassical eigenstates  $\Psi \propto \exp(W/\epsilon)$ . The semiclassical Hamiltonian is

$$-m(q, t)(\cos p - 1) + V(q, t), \quad (\text{B12})$$

where the effective  $q$  dependent mass is

$$m(q, t) = A(t) \sqrt{1 - q^2} / \epsilon. \quad (\text{B13})$$

Using the instanton technique, the gap can be estimated as

$$R \exp\left(-\frac{1}{\epsilon} \int_{q_a}^{q_b} dq p(q)\right), \quad (\text{B14})$$

where the exponent is the Euclidean action and  $p(q)$  is the instanton trajectory between the double-well minima  $q_a$  and  $q_b$ . The instanton trajectory is obtained by going to imaginary time (mapping  $p \rightarrow -ip$ ) and solving  $p(q)$  in Eq. (B12) to obtain

$$m(q, t)(1 - \cosh p) + V(q, t) = V(q_a, t). \quad (\text{B15})$$

We obtain

$$p(q) = \cosh^{-1}\left(\frac{V(q, t) - V(q_a, t)}{m(q, t)} + 1\right). \quad (\text{B16})$$

For the WKB attempt rate  $R$  we use the separation between the first and third eigenstates of the quantum Hamiltonian,  $R \approx 3$  GHz, as a proxy for the gap of the possible single well bound states. Plugging into Eq. (B14), we obtain a sufficient qualitative agreement with the exact gaps

$h_1$	exact gap	instanton gap
0.48	10 MHz	5 MHz
0.47	36 MHz	33 MHz
0.46	78 MHz	85 MHz

(B17)

The agreement improves for increasing  $n$  [6, 47, 75]

## Appendix C: Further comparisons of larger problems that contain the weak-strong cluster “motives” as subproblems.

### 1. SVMC and PIMC-QA results compared against D-Wave results

Figs. 27-32 show comparisons of SVMC (with and without  $\chi$ -correction) and PIMC-QA against D-Wave results on the larger problems that contain the weak-strong cluster “motives” as subproblems. At each problem size (40, 80, 120, 160, and 200 spins) we tested 100 random instances. D-Wave was executed with 16 gauges at each instance. SVMC and PIMC-QA were each executed with 9 different parameters settings: 3 values for *steps* and 3 values for  $\beta$ . The total number of sweeps is  $1000 \times \text{steps}$ . Each sweep attempts to update all qubits or spins in the problem instance. The plotted results were obtained by bootstrapping over the success probabilities obtained from individual instances and the error bars represent the bootstrapped estimate of standard error. The standard Student’s T-test ( $\alpha = 0.05$ ) was applied to verify the statistical significance of the difference in means between SVMC/PIMC-QA and D-Wave results. The null hypothesis was rejected at all parameter settings except for SVMC with  $\chi$ -correction and *steps* = 512, *beta* = 2.4, *size* = 5 on the problem without strong fields.

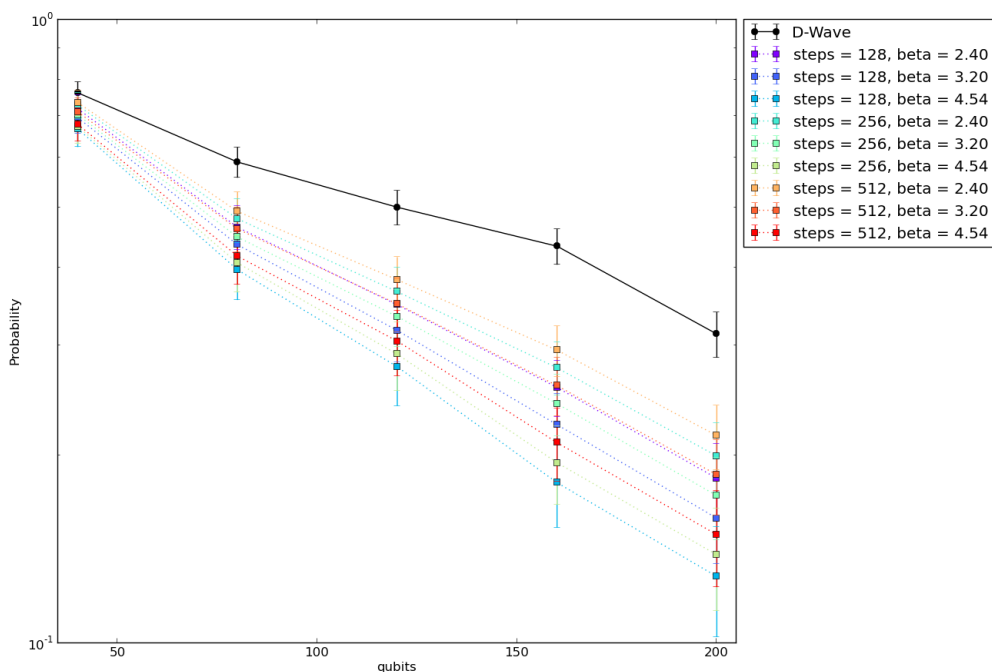


FIG. 27. D-Wave and SVMC (without  $\chi$ -correction) results for instances without strong fields.

### 2. Fitting curves

In order to obtain a rough estimate of scaling behavior, we performed bootstrapped linear fits on the logs of success probabilities obtained from the same instances whose results are shown in Figs. 27-32.

The resulting exponential fits in linear probability space for D-Wave are:

- Without strong fields:  $y(x) = e^{-0.0710 \pm 0.0573} e^{(-0.0052 \pm 0.0005)x}$
- With strong fields:  $y(x) = e^{-0.1174 \pm 0.0498} e^{(-0.0110 \pm 0.0005)x}$

Additionally, Tables I-VI show the corresponding fitting coefficients (in log probability space) done also on the SVMC and PIMC-QA results.

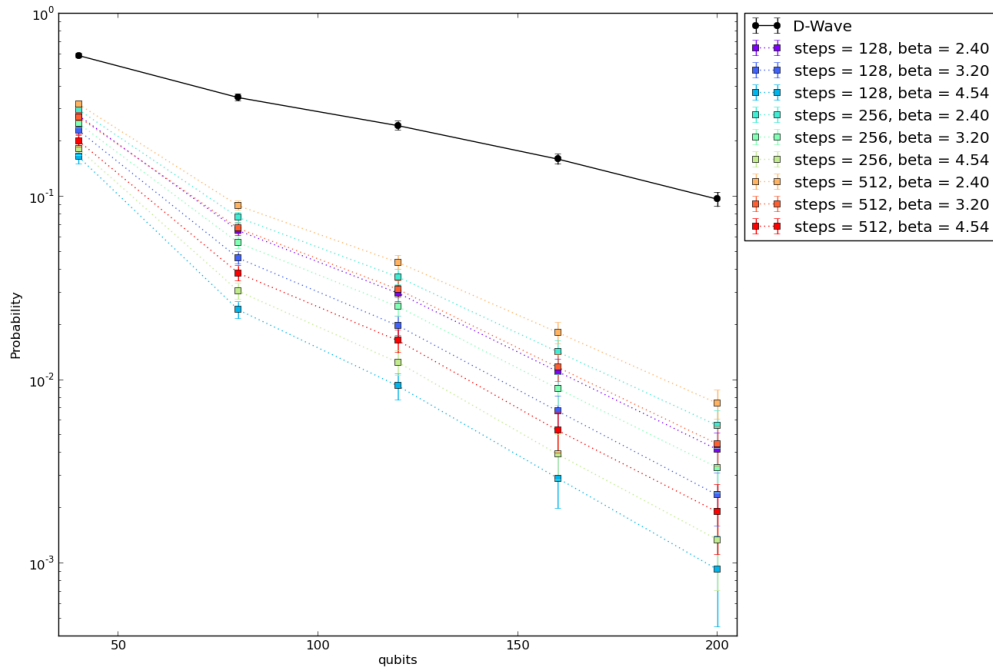


FIG. 28. D-Wave and SVMC (without  $\chi$ -correction) results for instances with strong fields.

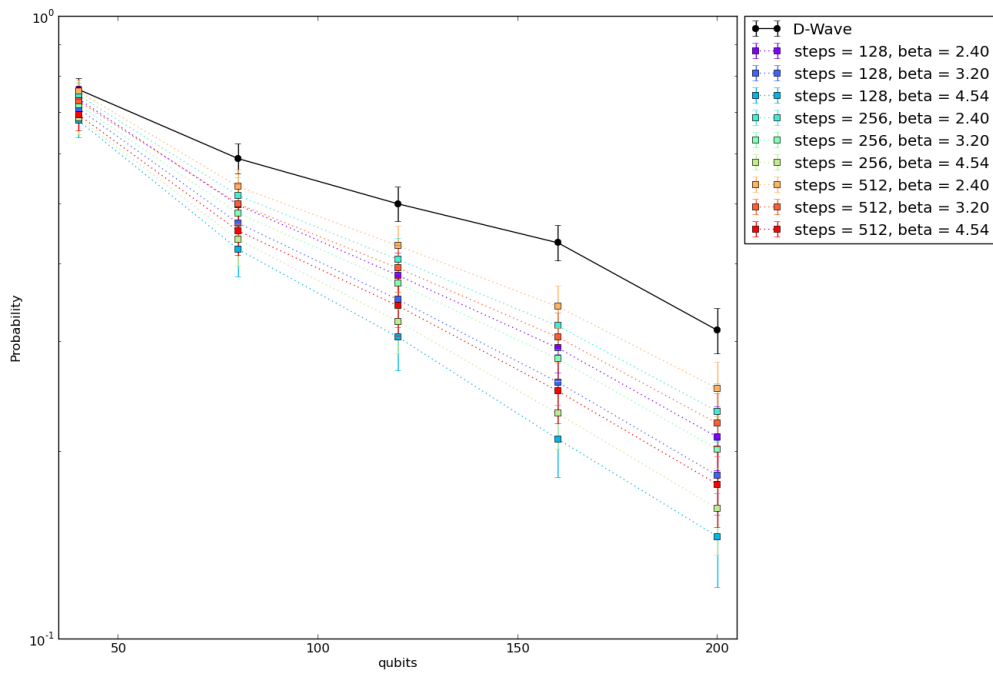


FIG. 29. D-Wave and SVMC (with  $\chi$ -correction) results for instances without strong fields.

Based on these fits, the ratios between scalings of SVMC/PIMC-QA and corresponding scalings of D-Wave were computed and are summarized as follows:

- Without strong fields
  - Ratios between SVMC without  $\chi$ -correction and D-Wave

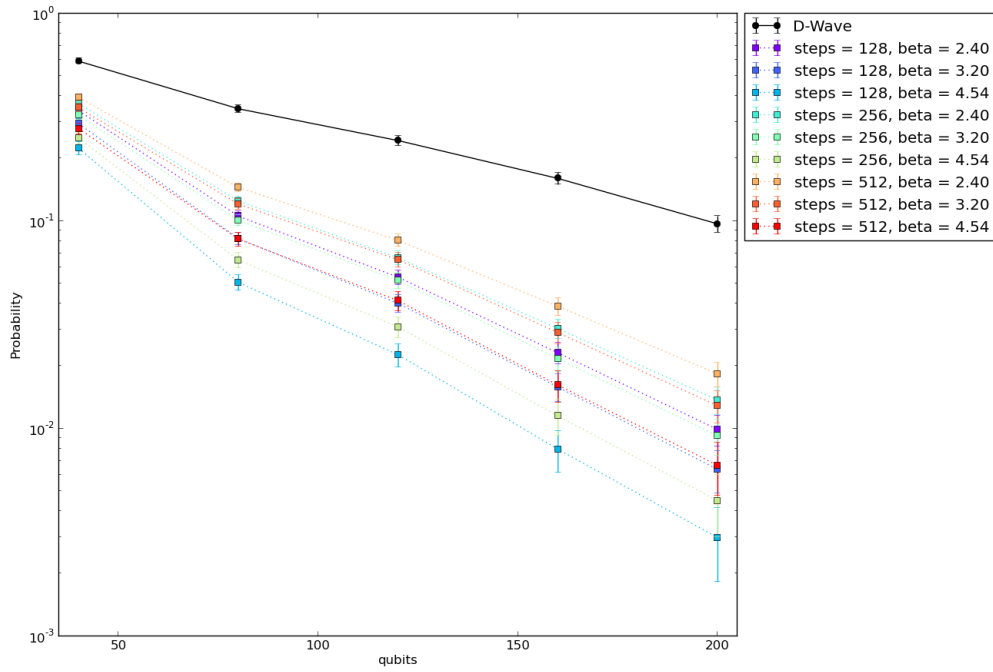


FIG. 30. D-Wave and SVMC (with  $\chi$ -correction) results for instances with strong fields.

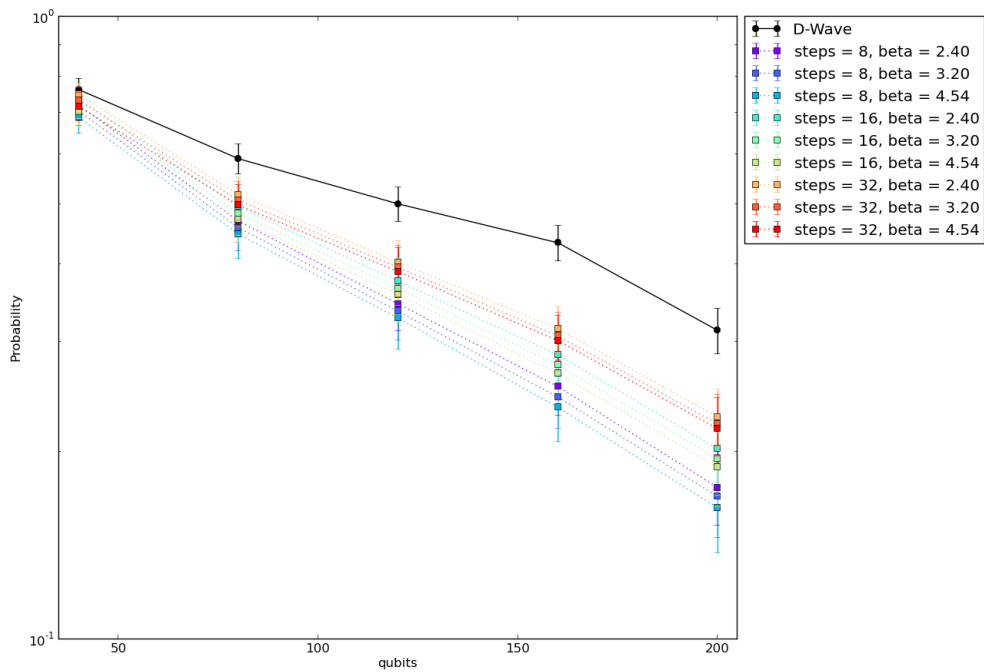


FIG. 31. D-Wave and PIMC-QA results for instances without strong fields.

- \* Min: 1.4423 (at  $steps = 512$ ,  $\beta = 2.4$ )
- \* Max: 1.9808 (at  $steps = 128$ ,  $\beta = 4.54$ )
- Ratios between SVMC with  $\chi$ -correction and D-Wave
  - \* Min: 1.2692 (at  $steps = 512$ ,  $\beta = 2.4$ )
  - \* Max: 1.8269 (at  $steps = 128$ ,  $\beta = 4.54$ )



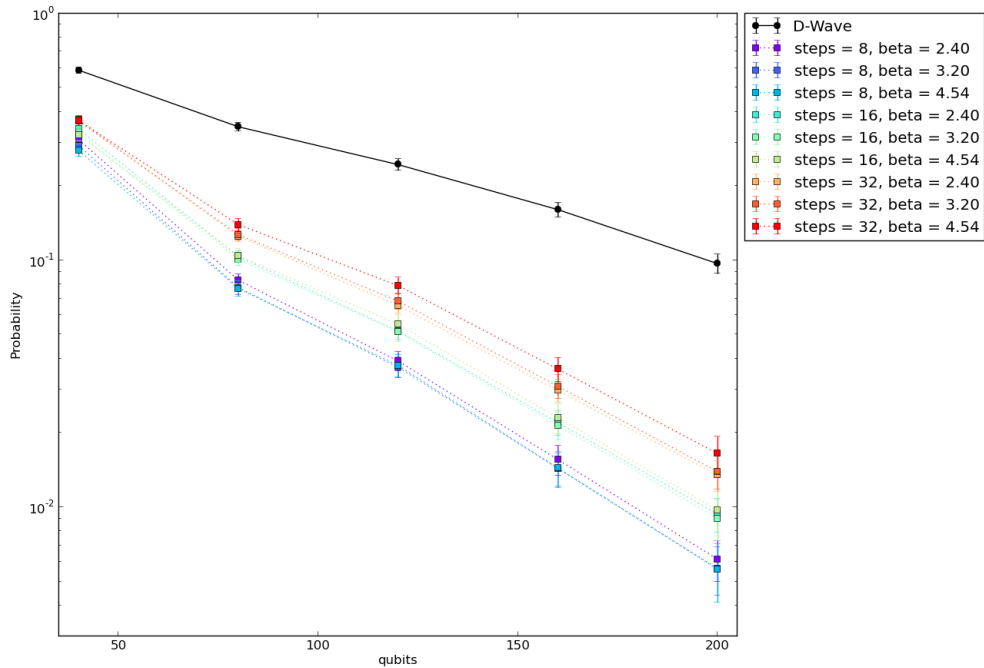


FIG. 32. D-Wave and PIMC-QA results for instances with strong fields.

steps\β	2.4	3.2	4.54
128	$(-0.0083 \pm 0.0008) * x - 0.0430 \pm 0.0823$	$(-0.0091 \pm 0.0009) * x - 0.0480 \pm 0.0948$	$(-0.0103 \pm 0.0012) * x - 0.0440 \pm 0.1146$
256	$(-0.0079 \pm 0.0008) * x - 0.0491 \pm 0.0783$	$(-0.0086 \pm 0.0009) * x - 0.0561 \pm 0.0903$	$(-0.0098 \pm 0.0011) * x - 0.0552 \pm 0.1102$
512	$(-0.0075 \pm 0.0007) * x - 0.0533 \pm 0.0744$	$(-0.0082 \pm 0.0008) * x - 0.0617 \pm 0.0856$	$(-0.0094 \pm 0.0010) * x - 0.0633 \pm 0.1050$

TABLE I. SVMC without  $\chi$ -correction and without strong fields

steps\β	2.4	3.2	4.54
128	$(-0.0255 \pm 0.0012) * x - 0.4461 \pm 0.1065$	$(-0.0280 \pm 0.0017) * x - 0.5607 \pm 0.1471$	$(-0.0320 \pm 0.0029) * x - 0.8125 \pm 0.2404$
256	$(-0.0242 \pm 0.0011) * x - 0.4118 \pm 0.0961$	$(-0.0265 \pm 0.0015) * x - 0.5150 \pm 0.1300$	$(-0.0304 \pm 0.0026) * x - 0.7377 \pm 0.2167$
512	$(-0.0229 \pm 0.0010) * x - 0.3810 \pm 0.0880$	$(-0.0251 \pm 0.0013) * x - 0.4689 \pm 0.1157$	$(-0.0287 \pm 0.0023) * x - 0.6755 \pm 0.1907$

TABLE II. SVMC without  $\chi$ -correction and with strong fields

steps\β	2.4	3.2	4.54
128	$(-0.0076 \pm 0.0007) * x - 0.0402 \pm 0.0729$	$(-0.0083 \pm 0.0008) * x - 0.0495 \pm 0.0843$	$(-0.0095 \pm 0.0010) * x - 0.0519 \pm 0.1026$
256	$(-0.0071 \pm 0.0006) * x - 0.0451 \pm 0.0682$	$(-0.0077 \pm 0.0008) * x - 0.0567 \pm 0.0790$	$(-0.0089 \pm 0.0009) * x - 0.0640 \pm 0.0972$
512	$(-0.0066 \pm 0.0006) * x - 0.0483 \pm 0.0639$	$(-0.0072 \pm 0.0007) * x - 0.0618 \pm 0.0742$	$(-0.0083 \pm 0.0009) * x - 0.0726 \pm 0.0916$

TABLE III. SVMC with  $\chi$ -correction and without strong fields

steps\β	2.4	3.2	4.54
128	$(-0.0215 \pm 0.0009) * x - 0.3469 \pm 0.0830$	$(-0.0234 \pm 0.0013) * x - 0.4257 \pm 0.1095$	$(-0.0267 \pm 0.0021) * x - 0.6079 \pm 0.1764$
256	$(-0.0200 \pm 0.0008) * x - 0.3166 \pm 0.0744$	$(-0.0217 \pm 0.0011) * x - 0.3830 \pm 0.0962$	$(-0.0248 \pm 0.0018) * x - 0.5419 \pm 0.1535$
512	$(-0.0187 \pm 0.0007) * x - 0.2868 \pm 0.0672$	$(-0.0202 \pm 0.0010) * x - 0.3438 \pm 0.0857$	$(-0.0229 \pm 0.0015) * x - 0.4808 \pm 0.1327$

TABLE IV. SVMC with  $\chi$ -correction and with strong fields

- Ratios between PIMC-QA and D-Wave
  - \* Min: 1.3846 (at  $steps = 32, \beta = 2.4$ )
  - \* Max: 1.7115 (at  $steps = 8, \beta = 4.54$ )

- With strong fields

steps\β	2.4	3.2	4.54
8	$(-0.0086 \pm 0.0008) * x - 0.0186 \pm 0.0795$	$(-0.0088 \pm 0.0008) * x - 0.0346 \pm 0.0860$	$(-0.0089 \pm 0.0009) * x - 0.0522 \pm 0.0934$
16	$(-0.0079 \pm 0.0007) * x - 0.0284 \pm 0.0730$	$(-0.0080 \pm 0.0008) * x - 0.0451 \pm 0.0791$	$(-0.0080 \pm 0.0008) * x - 0.0645 \pm 0.0859$
32	$(-0.0072 \pm 0.0006) * x - 0.0353 \pm 0.0674$	$(-0.0073 \pm 0.0007) * x - 0.0520 \pm 0.0724$	$(-0.0072 \pm 0.0007) * x - 0.0746 \pm 0.0778$

TABLE V. PIMC-QA without strong fields

steps\β	2.4	3.2	4.54
8	$(-0.0238 \pm 0.0010) * x - 0.3787 \pm 0.0906$	$(-0.0241 \pm 0.0012) * x - 0.4207 \pm 0.1063$	$(-0.0239 \pm 0.0014) * x - 0.4530 \pm 0.1232$
16	$(-0.0219 \pm 0.0009) * x - 0.3369 \pm 0.0792$	$(-0.0220 \pm 0.0010) * x - 0.3587 \pm 0.0904$	$(-0.0214 \pm 0.0012) * x - 0.3822 \pm 0.1036$
32	$(-0.0202 \pm 0.0008) * x - 0.3012 \pm 0.0705$	$(-0.0200 \pm 0.0009) * x - 0.3122 \pm 0.0772$	$(-0.0190 \pm 0.0009) * x - 0.3147 \pm 0.0850$

TABLE VI. PIMC-QA with strong fields

- Ratios between SVMC without  $\chi$ -correction and D-Wave
  - \* Min: 2.0818 (at  $steps = 512$ ,  $\beta = 2.4$ )
  - \* Max: 2.9091 (at  $steps = 128$ ,  $\beta = 4.54$ )
- Ratios between SVMC with  $\chi$ -correction and D-Wave
  - \* Min: 1.7000 (at  $steps = 512$ ,  $\beta = 2.4$ )
  - \* Max: 2.4273 (at  $steps = 128$ ,  $\beta = 4.54$ )
- Ratios between PIMC-QA and D-Wave
  - \* Min: 1.7273 (at  $steps = 32$ ,  $\beta = 4.54$ )
  - \* Max: 2.1909 (at  $steps = 8$ ,  $\beta = 3.2$ )

#### Appendix D: Chi probe for SVMC

The single qubit Hilbert space modeled as a spin vector in the SVMC numerics is obtained from the two lowest energy wave functions of the continuous flux qubit Hamiltonian with zero flux body bias (see App. A). For sufficiently high flux body bias, these two wavefunctions mix with higher energy wavefunctions of the continuous flux qubit Hamiltonian. We have checked that, up to the freezing point, the flux bias remains low for the problems that we study in this paper. Nevertheless, a model introduced by D-Wave to deal with this error has been treated as a fitting parameter for SVMC numerics in previous works [42, 45]. Our own derivation of this model gives the following equations modifying the couplings and local fields of the original Hamiltonian

$$h'_i = h_i - \chi \sum_j J_{ij} h_j \quad (D1)$$

$$J'_{ij} = J_{ij} - 2\chi \sum_k J_{ik} J_{kj} . \quad (D2)$$

While these equations are slightly different from those used in other works [42, 45], their effect is the same for the problems under study here. Explicitly, the problem becomes more ferromagnetic, and this has the effect of decreasing the barrier height for  $h_1 < J/2$ .

We want to constrain the possible values of  $\chi$  to be consistent with SVMC when  $\chi$  is treated as a fitting parameter. To this effect we introduce a “chi-probe” problem related to the weak-strong cluster motif, but without a multi-spin energy barrier. We also introduce many extra nearest-neighbor ferromagnetic couplings to increase the sensitivity cross-talk of Eq. (D2). Figure 33a shows the layout of this problem. Figure 33b shows the D-Wave data success probabilities and SVMC success probabilities for the “chi-probe” problems. The minimum residual error is found for  $\chi = 0.0025$ , and we use this value of  $\chi$  in the main text when appropriate. Because our factor of 2 in Eq. (D2) this value of  $\chi$  is roughly equivalent to a value of 0.05 for the equations used in Ref. [42].

Figure 34 shows a comparison of D-Wave data and SVMC numerics with  $\chi = 0.0025$  (compare with Fig. 18). As explained in the text, we choose 128,000 sweeps for an algorithmic temperature of 15 mK. Crucially, the temperature dependence is still the opposite for SVMC with  $\chi$  than for the D-Wave data, as expected. Figure 35a shows the success probability as a function of temperature for D-Wave, open system quantum numerics and the classical-path model (SVMC) for  $h_1 = 0.44$  in the Hamiltonian of Eq. (4). We include SVMC with  $\chi = 0.0025$ . The probability of success is higher for SVMC with than without  $\chi$ . The reason is that the problem modified with  $\chi$  is more ferromagnetic: it has an effectively lower ratio  $h_1/J$ . Nevertheless, the probability of success for SVMC with  $\chi$  is still lower than the probability of success for D-Wave. Figure 35b shows the probability of success versus  $h_1 = [0.3, \dots, 0.48]$ .

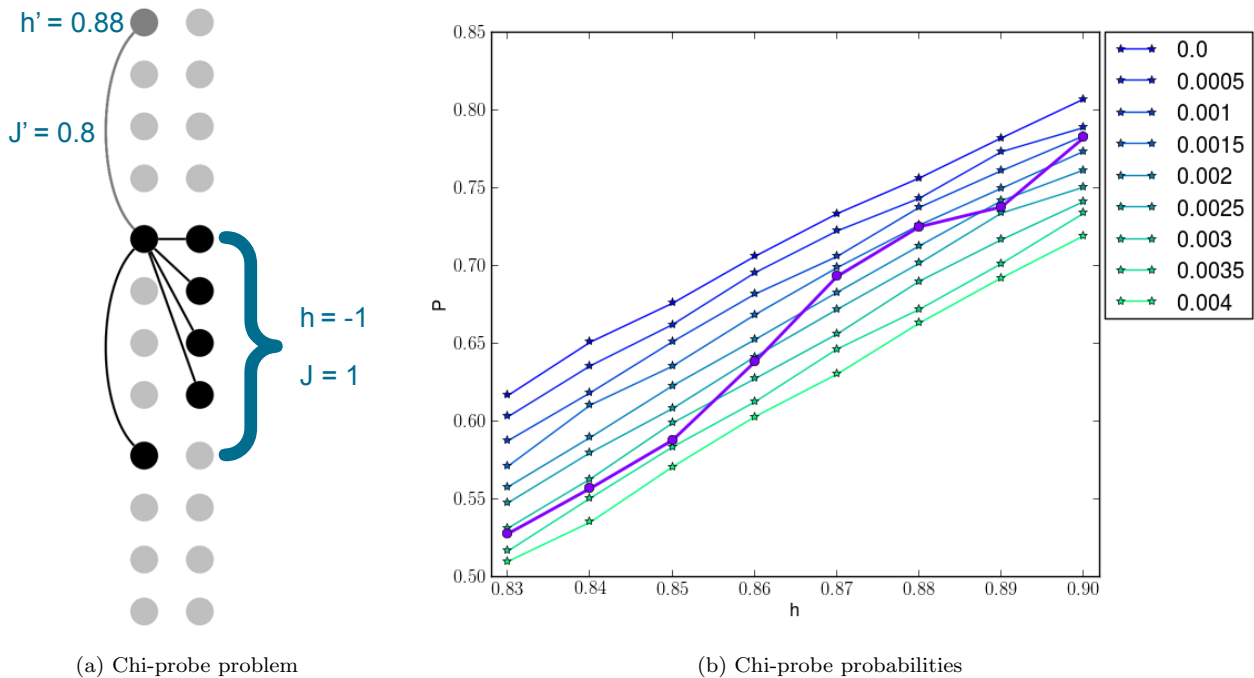


FIG. 33. Problem to constraint values of  $\chi$  compatible with SVMC. (a) Layout of the problem. (b) D-Wave data success probabilities (thicker line with  $\circ$  markers) and SVMC success probability for the “chi-probe” problems. The lines with  $\star$  markers correspond to SVMC with different values of  $\chi$ , from 0 to 0.004. The minimum residual error is found for  $\chi = 0.0025$ . We use SVMC with 125K sweeps and  $T=15$  mK, as explained in the main text.

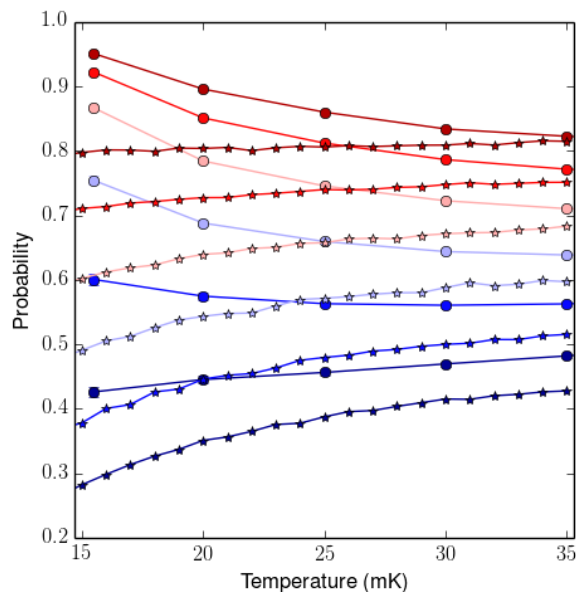


FIG. 34. Probability of success versus temperature for D-Wave data ( $\circ$  markers) and SVMC numerics ( $\diamond$  markers). We plot (from top to bottom, and red to blue)  $h_1 = [0.38, 0.4, 0.42, 0.44, 0.46, 0.48]$ . Error bars are smaller than markers. We use SVMC with  $\chi = 0.0025$  and 15 mK algorithmic temperature for 128,000 sweeps, as explained in the text.

- [1] G. Gamow, *Z. Physik* **51** (1928).  
 [2] R. H. Fowler and L. Nordheim, in *Proceedings of the Royal Society of London A: Mathematical, Physical and Engineering Sciences*, Vol. 119 (The Royal Soci-

- ety, 1928) pp. 173–181.  
 [3] A. B. Finnila, M. A. Gomez, C. Sebenik, C. Stenson, and J. D. Doll, *Chem. Phys. Lett.* **219**, 343 (1994).  
 [4] T. Kadowaki and H. Nishimori, *Phys. Rev. E* **58**, 5355

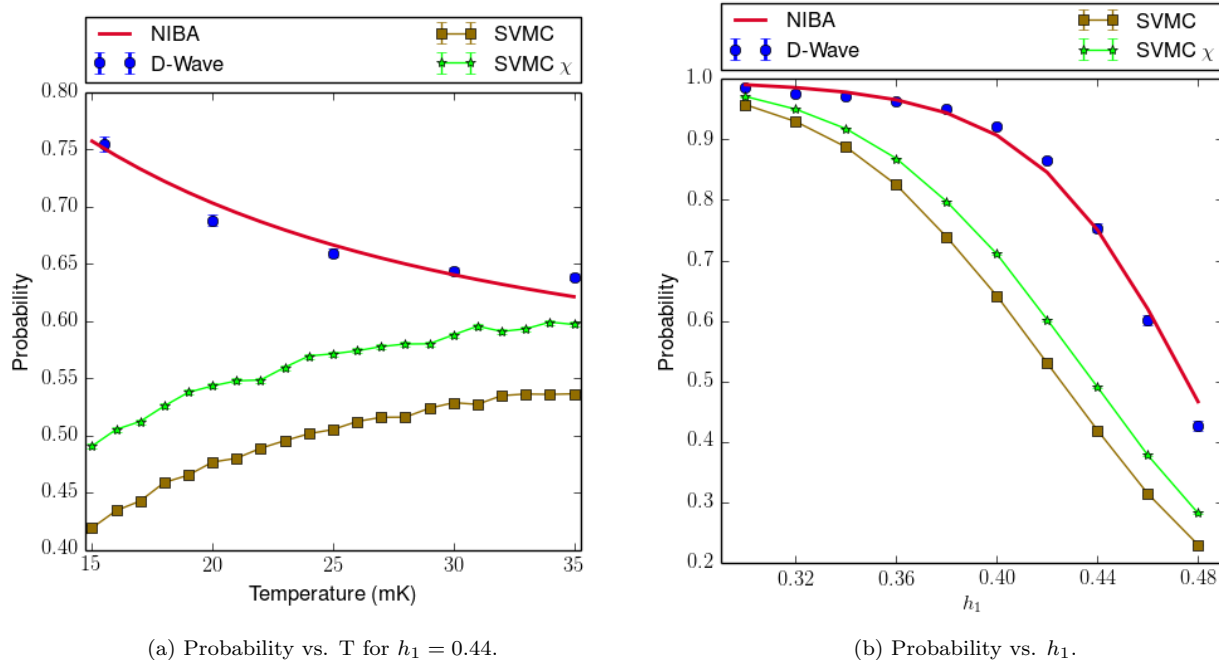


FIG. 35. Plots including SVMC with  $\chi = 0.0025$  for the double-well potential problem introduced in the main text. (a) Probability of success versus temperature at  $h_1 = 0.44$  for D-Wave (purple  $\circ$  marker), the NIBA Quantum Master Equations (continuous red line) and the classical-path model (SVMC). The two SVMC curves correspond to SVMC (brown  $\square$  marker) and SVMC with  $\chi = 0.0025$  (green  $\star$  marker). (b) Probability of success versus  $h_1$ . Error bars are smaller than markers.

- (1998).
- [5] J. Brooke, D. Bitko, T. F. Rosenbaum, and G. Aeppli, *Science* **284**, 779 (1999).
  - [6] E. Farhi, J. Goldstone, and S. Gutmann, arXiv:quant-ph/0201031 (2002).
  - [7] G. E. Santoro, R. Martoňák, E. Tosatti, and R. Car, *Science* **295**, 2427 (2002).
  - [8] A. C. Seabaugh and Q. Zhang, *Proceedings of the IEEE* **98**, 2095 (2010).
  - [9] G. Binnig and H. Rohrer, *IBM Journal of research and development* **44**, 279 (2000).
  - [10] M. Mohseni, Y. Omar, G. S. Engel, and M. B. Plenio, *Quantum effects in biology* (Cambridge University Press, 2014).
  - [11] D. L. Klein, R. Roth, A. K. Lim, A. P. Alivisatos, and P. L. McEuen, *Nature* **389**, 699 (1997).
  - [12] D. Gatteschi and R. Sessoli, *Phys. Rev. Lett.* **60**, 661 (1988).
  - [13] A. Leggett, in *NATO ASI Series E: Applied Sciences*, Vol. 301, edited by B. B. L. Gunther (Kluwer, Dordrecht, 1995).
  - [14] D. Gatteschi and R. Sessoli, *Angew. Chem. Int. Ed* **42**, 268 (2003).
  - [15] E. Burzur, F. Luis, B. Barbara, R. Ballou, E. Ressouche, O. Montero, J. Campo, and S. Maegawa, *Phys. Rev. Letters* **107** (2011), 10.1103/PhysRevLett.107.097203.
  - [16] I. Eichwald, S. Bretkreutz, G. Ziemys, G. Csaba, W. Porod, and M. Becherer, *Science* **311**, 5758 (2014).
  - [17] I. Eichwald, S. Bretkreutz, G. Ziemys, G. Csaba, W. Porod, and M. Becherer, *Nanotechnology* **25**, 335202 (2014).
  - [18] C. Sangregorio, T. Ohm, C. Paulsen, R. Sessoli, and D. Gatteschi, *Phys. Rev. Lett.* **78**, 4645 (1997).
  - [19] M. Soler, W. Wernsdorfer, K. Folting, M. Pink, and G. Christou, *J. Am. Chem. Soc* **126**, 2156 (2004).
  - [20] P. Ray, B. K. Chakrabarti, and A. Chakrabarti, *Phys. Rev. B* **39**, 11828 (1989).
  - [21] M. Johnson, M. Amin, S. Gildert, T. Lanting, F. Hamze, N. Dickson, R. Harris, A. Berkley, J. Johansson, P. Bunyk, *et al.*, *Nature* **473**, 194 (2011).
  - [22] T. Lanting, R. Harris, J. Johansson, M. H. S. Amin, A. J. Berkley, S. Gildert, M. W. Johnson, P. Bunyk, E. Tolkacheva, E. Ladizinsky, N. Ladizinsky, T. Oh, I. Perminov, E. M. Chapple, C. Enderud, C. Rich, B. Wilson, M. C. Thom, S. Uchaikin, and G. Rose, *Phys. Rev. B* **82**, 060512 (2010).
  - [23] E. Farhi, J. Goldstone, S. Gutmann, J. Lapan, A. Lundgren, and D. Preda, *Science* **292**, 472 (2001).
  - [24] R. Harris, J. Johansson, A. J. Berkley, M. W. Johnson, T. Lanting, S. Han, P. Bunyk, E. Ladizinsky, T. Oh, I. Perminov, E. Tolkacheva, S. Uchaikin, E. M. Chapple, C. Enderud, C. Rich, M. Thom, J. Wang, B. Wilson, and G. Rose, *Phys. Rev. B* **81**, 134510 (2010).
  - [25] R. Harris, M. W. Johnson, T. Lanting, A. J. Berkley, J. Johansson, P. Bunyk, E. Tolkacheva, E. Ladizinsky, N. Ladizinsky, T. Oh, F. Cioata, I. Perminov, P. Spear, C. Enderud, C. Rich, S. Uchaikin, M. C. Thom, E. M. Chapple, J. Wang, B. Wilson, M. H. S. Amin, N. Dickson, K. Karimi, B. Macready, C. J. S. Truncik, and G. Rose, *Phys. Rev. B* **82**, 024511 (2010).
  - [26] J. M. Martinis, K. B. Cooper, R. McDermott, M. Steffen, M. Ansmann, K. D. Osborn, K. Cicak, S. Oh, D. P. Pappas, R. W. Simmonds, and C. C. Yu, *Phys. Rev. Lett.* **95**, 210503 (2005).
  - [27] L. Faoro and L. Ioffe, *Phys. Rev. Lett.* , 227995 (2008).
  - [28] E. Paladino, Y. Galperin, G. Falci, and B. Altshuler, *Ref. Mod. Phys.* **86**, 361 (2014).
  - [29] P. Ao and J. Rammer, *Phys. Rev. Lett.* **62**, 3004

- (1989).
- [30] Y. Kayanuma and H. Nakayama, *Physics Review B* **57**, 13099 (1998).
- [31] T. Lanting, M. H. S. Amin, M. W. Johnson, F. Altomare, A. J. Berkley, S. Gildert, R. Harris, J. Johansson, P. Bunyk, E. Ladizinsky, E. Tolkacheva, and D. V. Averin, *Phys. Rev. B* **83**, 180502 (2011).
- [32] S. Boixo, T. Albash, F. M. Spedalieri, N. Chancellor, and D. A. Lidar, *Nat. Commun.* **4** (2013).
- [33] N. Dickson, M. Johnson, M. Amin, R. Harris, F. Altomare, A. Berkley, P. Bunyk, J. Cai, E. Chapple, P. Chavez, *et al.*, *Nat. Commun.* **4**, 1903 (2013).
- [34] C. C. McGeoch and C. Wang, in *Proceedings of the ACM International Conference on Computing Frontiers* (ACM, 2013) p. 23.
- [35] S. Dash, arXiv:1306.1202 (2013).
- [36] S. Boixo, T. F. Rønnow, S. V. Isakov, Z. Wang, D. Wecker, D. A. Lidar, J. M. Martinis, and M. Troyer, *Nat. Phys.* **10**, 218 (2014).
- [37] T. Lanting, A. Przybysz, A. Y. Smirnov, F. Spedalieri, M. Amin, A. Berkley, R. Harris, F. Altomare, S. Boixo, P. Bunyk, *et al.*, *Phys. Rev. X* **4**, 021041 (2014).
- [38] S. Santra, G. Quiroz, G. Ver Steeg, and D. A. Lidar, *New J. Phys.* **16**, 045006 (2014).
- [39] T. F. Rønnow, Z. Wang, J. Job, S. Boixo, S. V. Isakov, D. Wecker, J. M. Martinis, D. A. Lidar, and M. Troyer, *Science* **345**, 420 (2014).
- [40] W. Vinci, K. Markström, S. Boixo, A. Roy, F. M. Spedalieri, P. A. Warburton, and S. Severini, *Sci. Rep.* **4** (2014).
- [41] S. W. Shin, G. Smith, J. A. Smolin, and U. Vazirani, arXiv:1401.7087 (2014).
- [42] W. Vinci, T. Albash, A. Mishra, P. A. Warburton, and D. A. Lidar, arXiv:1403.4228 (2014).
- [43] C. C. McGeoch, *Synthesis Lectures on Quantum Computing* **5**, 1 (2014).
- [44] D. Venturelli, S. Mandrà, S. Knysh, B. O’Gorman, R. Biswas, and V. Smelyanskiy, arXiv:1406.7553 (2014).
- [45] T. Albash, T. F. Rønnow, M. Troyer, and D. A. Lidar, arXiv:1409.3827 (2014).
- [46] A. D. King and C. C. McGeoch, arXiv:1410.2628 (2014).
- [47] A. Boulatov and V. N. Smelyanskiy, *Phys. Rev. A* **68** (2003), 10.1103/PhysRevA.68.062321.
- [48] F. K. Wilhelm, M. J. Storz, U. Hartmann, and M. R. Geller, in *Manipulating Quantum Coherence in Solid State Systems*, Vol. 244 (Springer Netherlands, 2007) pp. 195–232.
- [49] T. Albash, S. Boixo, D. A. Lidar, and P. Zanardi, *New J. Phys.* **14**, 123016 (2012).
- [50] A. J. Leggett, S. Chakravarty, A. T. Dorsey, M. P. A. Fisher, A. Garg, and W. Zwerger, *Ref. Mod. Phys.* **59**, 1 (1987).
- [51] M. S. Sarandy and D. A. Lidar, *Phys. Rev. Lett* **95**, 250503 (2005).
- [52] M. S. Sarandy and D. A. Lidar, *Phys. Rev. A* **95**, 012331 (2005).
- [53] M. Amin, P. Love, and C. Truncik, *Phys. Rev. Lett* **100**, 06050 (2008).
- [54] I. de Vega, M. C. Banuls, and A. Pérez, *Phys. Rev. Lett* **12**, 123010 (2010).
- [55] M. Amin, C. Truncik, and D. Averin, *Phys. Rev. A* **80**, 022303 (2009).
- [56] S. Sendelbach, D. Hover, A. Kittel, M. Mck, J. M. Martinis, and R. McDermott, *Phys. Rev. B* **67**, 094510 (2003).
- [57] D. V. Harlingen, T. Robertson, B. Plourde, P. Reichardt, T. Crane, and J. Clarke, *Phys. Rev. B* **70**, 064517 (2004).
- [58] S. Sendelbach, D. Hover, A. Kittel, M. Mck, J. M. Martinis, and R. McDermott, *Phys. Rev. Lett.* **100**, 227006 (2008).
- [59] J. Bylander, S. Gustavsson, F. Yan, F. Yoshihara, K. Harrabi, G. Fitch, D. G. Cory, Y. Nakamura, J.-S. Tsai, and W. D. Oliver, *Nat. Phys.* **7**, 565 (2011).
- [60] F. Yan, J. Bylander, S. Gustavsson, F. Yoshihara, K. Harrabi, D. G. Cory, T. P. Orlando, Y. Nakamura, J.-S. Tsai, and W. D. Oliver, *Phys. Rev. B* **85**, 17452 (2012).
- [61] F. Yoshihara, Y. Nakamura, F. Yan, S. Gustavsson, J. Bylander, W. D. Oliver, and J.-S. Tsai, *Phys. Rev. B* **89**, 020503 (2014).
- [62] R. Harris, M. Johnson, S. Han, A. Berkley, J. Johansson, P. Bunyk, E. Ladizinsky, S. Govorkov, M. Thom, S. Uchaikin, B. Bumble, A. Fung, A. Kaul, A. Kleinsasser, M. Amin, and D. Averin, *Phys. Rev. Lett.* **101**, 117003 (2008).
- [63] M. H. S. Amin and D. V. Averin, *Phys. Rev. Lett.* **100**, 197001 (2008).
- [64] S. Pekar, *Zh. Expt. Th. Phys.* **20**, 510 (1950).
- [65] K. Huang and A. Rhys, *Proc. Royal Soc.* **204**, 406 (1950).
- [66] W. H. Zurek, *Phys. Rev. D* **24**, 1516 (1981).
- [67] P. Ao and J. Rammer, *Phys. Rev. B* **43**, 5397 (1991).
- [68] H. Dekker, *Physics Review A* **35**, 1436 (1987).
- [69] R. Marcus, *J. Chem. Phys.* **24**, 966 (1956).
- [70] V. L. Pokrovsky and D. Sun, *Phys. Rev. B* , 024310 (2007).
- [71] A. Abrikosov, L. Gorkov, and I. Dzyaloshinskii, *Methods of Quantum Field Theory in Statistical Physics* (Prentice Hall, New York, 1963).
- [72] P. Crowley, T. Duric, W. Vinci, P. Warburton, and A. Green, arXiv:1405.5185 (2014).
- [73] W. H. Zurek, *Prog. Theor. Phys.* , 281 (1993).
- [74] R. Harris, T. Lanting, A. J. Berkley, J. Johansson, M. W. Johnson, P. Bunyk, E. Ladizinsky, N. Ladizinsky, T. Oh, and S. Han, *Phys. Rev. B* **80**, 052506 (2009).
- [75] M. Enz and R. Schilling, *Journal of Physics C: Solid State Physics* **19**, 1765 (1986).